

Subaerial Profiles at Two Beaches: Equilibrium and Machine Learning

Mika Natalie Siegelman¹, Ryan A McCarthy¹, Adam Patrick Young¹, William O'Reilly², Hironori Matsumoto¹, Mele O Johnson¹, Connor Mack¹, and R.T. Guza¹

¹Scripps Institution of Oceanography

²University of California, San Diego

November 14, 2023

Abstract

Weekly to quarterly beach elevation surveys spanning 700-800 m alongshore and 8 years at two beaches were each supplemented with several months of 100 sub-weekly surveys. These beaches, which have different sediment types (sand vs. sand-cobble mix), both widen in summer in response to the seasonal wave climate, in agreement with a generic equilibrium model. Results suggest differences in backshore erodability contribute to differing beach responses in the stormiest (El Niño) year. At both sites, the time dependence of the equilibrium modeled shoreline resembles the first mode of an EOF decomposition of the observations. With sufficient training, an equilibrium-informed Extra Tree Regression model, that includes features motivated by equilibrium modelling, can significantly outperform a generic equilibrium model.

Subaerial Profiles at Two Beaches: Equilibrium and Machine Learning

M. N. Siegelman¹, R. A. McCarthy¹, A. P. Young¹, W. O'Reilly¹, H. Matsumoto¹, M. Johnson¹, C. Mack¹, and R. T. Guza¹

¹Scripps Institution of Oceanography, 9500 Gilman Drive, La Jolla, CA 92037 USA

Key Points:

- At two beaches, weekly to quarterly elevation surveys spanning 700-800 m along-shore and 8 years were supplemented with ~ 100 subweekly surveys spanning several months.
- The Equilibrium-informed Extra Tree (ET) Regression Machine Learning model uses features (e.g. 30 day wave energy anomaly) inspired by equilibrium concepts
- With sufficient training, ET outperforms a generic equilibrium model

Corresponding author: Mika N. Siegelman, msiegelman@ucsd.edu

Abstract

Weekly to quarterly beach elevation surveys spanning 700-800 m alongshore and 8 years at two beaches were each supplemented with several months of ~ 100 sub-weekly surveys. These beaches, which have different sediment types (sand vs. sand-cobble mix), both widen in summer in response to the seasonal wave climate, in agreement with a generic equilibrium model. Results suggest differences in backshore erodability contribute to differing beach responses in the stormiest (El Niño) year. At both sites, the time dependence of the equilibrium modeled shoreline resembles the first mode of an EOF decomposition of the observations. With sufficient training, an equilibrium-informed Extra Tree Regression model, that includes features motivated by equilibrium modelling, can significantly outperform a generic equilibrium model.

Plain Language Summary

Beach elevation surveys are compared at two beaches in San Diego County. Both beaches narrow during winter as large wave events transport sand offshore and widen during summer as gentle waves move sand onshore. The seasonality of such beaches has been characterized by simple models that primarily rely on wave energy relative to an average state to predict beach width changes, known as equilibrium models. Here, we highlight some of the limitations of equilibrium models, such as a tendency to over predict winter erosion at a beach backed by non-erodible infrastructure. We demonstrate that machine learning models, when trained with sufficient observations, can predict beach width changes more accurately than equilibrium models.

1 Introduction

Forecasting wave runup and overtopping depends on reliable estimates of future waves and nearshore bathymetry. Wave model forecasts are increasingly accurate on time scales ranging from several days to seasons. However, changes in beach bathymetry (e.g. shoreline location and beach slope) are understood poorly. Many authors emphasize the feedback between runup and evolving bathymetry, and the relative lack of comprehensive (in space and time) bathymetry observations for model validation (e.g. Straub et al. (2020); Henderson et al. (2022) and many others).

Using standardized calibration and test periods, Montaña et al. (2020) compared the performance of 12 “Equilibrium” and 7 ML models with designated calibration and testing periods at Tairua Beach in New Zealand. As a comparison baseline for errors, the data were detrended with no further adjustment. RMSE (root-mean-square-error) was never reduced by more than 20% from the baseline RMSE ≈ 5.3 m, and in most cases the error reduction was $< 10\%$ (Figure 3 in Montaña et al. (2020)). Overall, Equilibrium and ML models performed similarly with low skill. Blossier et al. (2017) report shoreline location errors at Tairua between +3.50 m and -4 m, suggesting that noise could have limited model skill. More recently, Gomez-de la Pena et al. (2023) compared Tairua observations with model results using complex neural network (CNN), hybrid CNN-LSTM, and equilibrium models. LSTMs extract sequential information and long-term temporal dependencies. Shoreline evolution is strongly seasonal, so the hybrid Gomez-de la Pena et al. (2023) model would be expected to outperform the memory-lacking CNN; however, CNN and hybrid models yielded similar RMSE. Gomez-de la Pena et al. (2023) review some of rapidly expanding applications of ML to shoreline change.

Process-based models, such as XBeach, Cshore, SBeach, and COAWST, often show skill in simulating erosion from individual storms when tuned with site-specific observations, but optimal parameter values can vary (unpredictably) in space and time (Kalligeris et al., 2020). Recovery is not reliably modeled, errors accumulate in long-term simulations, and process-based models have not been successfully used for years-long simula-

62 tions. Storm erosion is more accurately simulated with a neural network than with SBeach
63 or XBeach (Simmons & Splinter, 2022).

64 Equilibrium beach models, noteworthy for their numerical simplicity and relatively
65 few free parameters, quantify the hypotheses (Wright et al., 1985; Miller & Dean, 2004)
66 that for a constant wave field there is an equilibrium beach morphology (the equilibrium
67 beach) that would remain constant in time, neither eroding nor accreting. A beach in
68 disequilibrium with ambient waves changes towards the equilibrium shape at a rate pro-
69 portional to the disequilibrium: $\frac{dX_{MHW}}{dt} = C^\pm E^{1/2} \Delta E$, where E is wave energy, and
70 C^\pm are change rate coefficients. The energy disequilibrium, ΔE , is the difference between
71 the wave energy and an equilibrium energy, $E_{eq}(X_{MHW}) = aX_{MHW} + b$, where a and
72 b are fit to observations. The functional forms for $\frac{dX_{MHW}}{dt}$ and $E_{eq}(X_{MHW})$ are some-
73 what arbitrary and many variants of these forms have similar skill (Yates, Guza, & O’Reilly,
74 2009; Davidson et al., 2013).

75 When calibrated with observed waves and shoreline locations, equilibrium mod-
76 els qualitatively reproduce shoreline change on seasonal to interannual time scales (Miller
77 & Dean, 2004; Yates, Guza, & O’Reilly, 2009; Ruggiero et al., 2010; Davidson et al., 2013;
78 Ruggiero et al., 2013; Splinter et al., 2014; Ludka et al., 2015). Equilibrium models are
79 often used to simulate beach response to climate change (e.g. sea level rise) because of
80 their simplicity (Athanasίου et al., 2020; D’Anna et al., 2021) and lack of viable alter-
81 natives. Equilibrium models and ML are both data-driven. Equilibrium models make
82 sweeping assumptions that reduce the model complexity to a few (between 2 and 4) con-
83 stants in a first order differential equation. ML (as used here) is relatively assumption
84 free and allows unlimited model complexity.

85 In Section 2, we describe about 8 years of seasonal beach elevation surveys suppl-
86 emented with ~ 100 sub-weekly surveys spanning several months. Seasonal changes are
87 reproduced relatively well with an equilibrium model, but sub-weekly observations are
88 not. ML models are presented in section 3, and compared with observations and equi-
89 librium in section 4. Results are discussed in Section 5.

90 2 Study Site

91 Sand level observations span almost 8 years (2015-2022) and 600 m at Torrey Pines
92 State Beach (TP) and 500 m at north Black’s Beach (BN), separated by approximately
93 2.4 km (Figures 1 and 2). Wave buoys and models are used to hindcast and forecast hourly
94 waves on transects spaced 100 m, known as MOP lines (O’Reilly et al., 2016). TP con-
95 tains 7 MOP lines (578-584) and BN contains 6 (MOP 550-555) (Figure 1 and 2). Dur-
96 ing winter storms, the significant wave height, H_s , can reach ~ 4 m at both sites (Fig-
97 ure 2a,d). The spring tidal range is ~ 2 m.

98 2.1 Subaerial Sand Elevation

99 Subaerial beach surveys before 2017 were approximately quarterly with an ATV
100 mounted RTK GPS. Beginning in 2017, surveys collected with a truck mounted LiDAR
101 (RIEGL VMZ-2000 laser scanner) are gridded (1 m x 1 m) after removing the swash zone,
102 ground filtering, and manual noise removal. TP was usually surveyed on timescales rang-
103 ing from weekly to monthly but was surveyed weekly for the entirety of 2019. BN Li-
104 DAR surveys were usually quarterly with some monthly surveys (Figure 2, Matsumoto
105 and Young (2022)).

106 A cart mounted RTK GPS system surveyed along MOP transects from the back
107 beach to a target minimum elevation of 0.774 m (NAVD88, MSL) during high frequency
108 sampling (colored boxes in Figure 2), even when tides and waves were not low and the
109 survey area was in the inner surf zone (Figures 3 and 4). Daily TP (578-584) surveys spanned

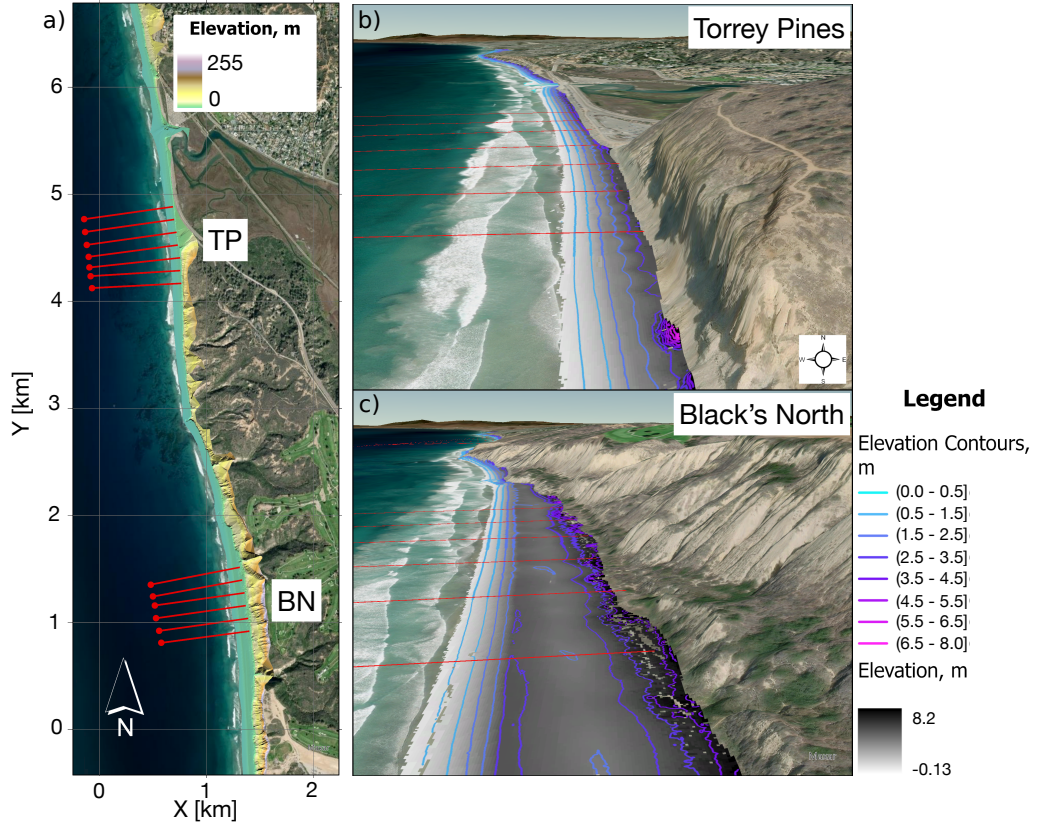


Figure 1. a) Torrey Pines (TP) and Black's North (BN) locations and (b,c) aerial photos. Cross-shore transects (solid red lines) are spaced 100 m alongshore. Elevation contours (legend) show a wide terrace at BN. Steep cliffs and riprap back the narrower TP, where beach cusps appear as alongshore periodic purple mounds at the cliff base and the 2.5-3.5 m contour location.

110 110 days from October 11, 2021 – February 3, 2022, with approximately a one week De-
 111 cember gap. BN (550-555) was surveyed every other day for 180 days from February 8,
 112 2022 – July 21, 2022 (Figure 3).

113 Free parameter values of Yates, Guza, and O'Reilly (2009), tuned at TP, are used
 114 here for both TP and BN. We use X_{MHW} rather than X_{MSL} (Yates, Guza, & O'Reilly,
 115 2009) because beach volume is better correlated with X_{MHW} than X_{MSL} (Section 2.2).
 116 Re-tuning model parameter values does not significantly improve model skill.

117 Southern California waves are relatively energetic during winter and calm during
 118 summer (Figure 2a,d). Both beaches widen during summer and narrow during winter,
 119 in agreement with a generic equilibrium model (Yates, Guza, and O'Reilly (2009), Fig-
 120 ure 2b,e, blue line). During summer, both beaches are primarily sandy (median diam-
 121 eter 0.25 mm (Yates, Guza, O'Reilly, & Seymour, 2009)). At TP, winter erosion often
 122 exposes cobble, sometimes as extensive cobble berms and cusps. (Matsumoto et al., 2020).

123 Shoreline responses in the stormiest year ('15/'16 El Niño, Figure 2, green arrows)
 124 differ. At TP, X_{MHW} plateaus at about the same location every winter, regardless of
 125 wave conditions. Doria et al. (2016) attributes the plateau to "erosion resistant bound-
 126 aries," including cliffs or rip rap and the cobble layer, which become exposed during the
 127 winter. In contrast, BN is backed by an erodible sand berm (Figure 4). A generic equi-
 128 librium lacks the complexity to include such details.

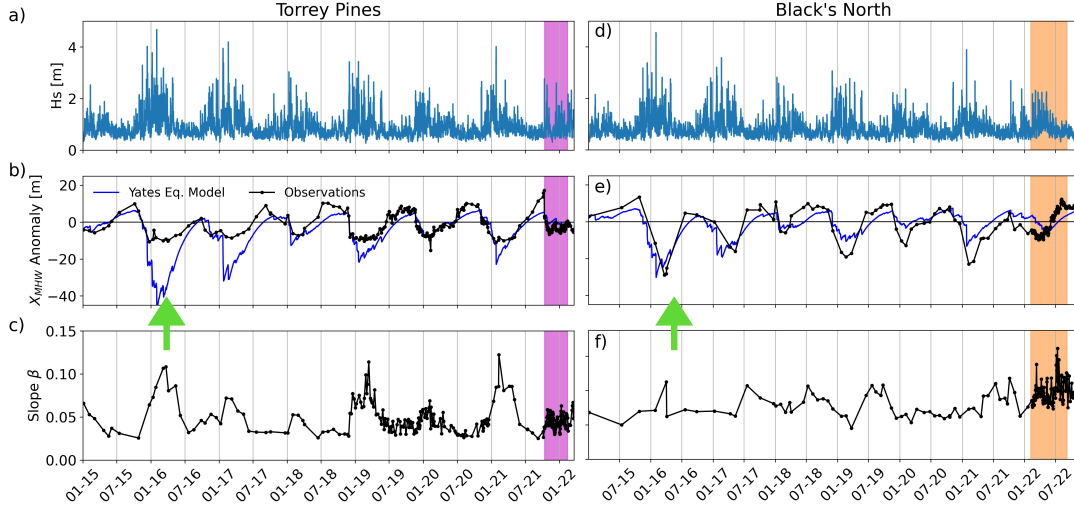


Figure 2. Left (Torrey Pines), right (Black's North) time series (almost 8 years) (a,d) significant wave height, H_s , in 10 m depth, (b,e) X_{MHW} anomaly (the cross-shore distance between the MHW contour and the mean (averaged over time and MOP lines at each beach). Equilibrium model (blue curve) uses constants (except for the mean shoreline location) from (Yates, Guza, & O'Reilly, 2009). Arrows mark 2016 winter when the BN sandy back beach retreated more than at cliff-backed TP. (c,f) slope, β , between MHW and MSL contours. Sub-weekly observations (vertical color bars) are detailed in Figure 3.

129 Despite the overall similar seasonal response of beach width to the wave conditions,
 130 the beach slope, β , (defined between X_{MSL} and X_{MHW}) response is opposite at BN and
 131 TP (Figure 2c,f). At TP, the summer, accreted profile has a gentle slope, whereas in BN's
 132 most accreted state, a prominent, steep-faced terrace forms between 50 m and 100 m from
 133 the back beach during the summer and spring. As the terrace erodes, the beach face re-
 134 retreats and the slope decreases.

135 During daily sampling at TP, two events with $H_s > 2.5$ m caused limited beach
 136 narrowing, consistent with an equilibrium model (days 12 and 60, Figure 3a). Between
 137 wave events, the observed and modeled beach weakly accrete. As winter continues (day
 138 80), the spread between MOP transects at TP increases possibly owing to composite sand-
 139 cobble cusps and megacusps. A similar pattern of increasing alongshore complexity over
 140 the course of the winter is observed with the weekly truck LiDAR (Matsumoto et al.,
 141 2020). The slope (between X_{MSL} and X_{MHW}) varied seasonally, but also with 14-day
 142 (spring-neap) period (Figure 3d,j) (Muñoz-Pérez & Medina, 2000; Phillips et al., 2017).
 143 Temporal EOF amplitudes of the observed X_{MHW} anomaly, Mode-1 EOF reconstruction,
 144 and equilibrium model are similar (Figure 3f,l). EOFs are discussed in Appendix
 145 A.

146 2.2 Subaerial Volume and Proxies

147 Historically, X_{MSL} , X_{MHW} and X_{MHHW} have all been used as shoreline reference
 148 contours for beach width (Sallenger et al., 2002; Farris & List, 2007; Yates, Guza, O'Reilly,
 149 & Seymour, 2009; Harley et al., 2011). Here, subaerial volumes, Vol , at BN and TP are
 150 more highly correlated with X_{MHW} and X_{MHHW} than with X_{MSL} (Figure 4c,d). X_{MHW}
 151 is used below (e.g. Figure 7) X_{MSL} is relatively unresponsive to volume changes high
 152 on the accreted profile. Furthermore, subaerial surveys of X_{MHW} can be measured with

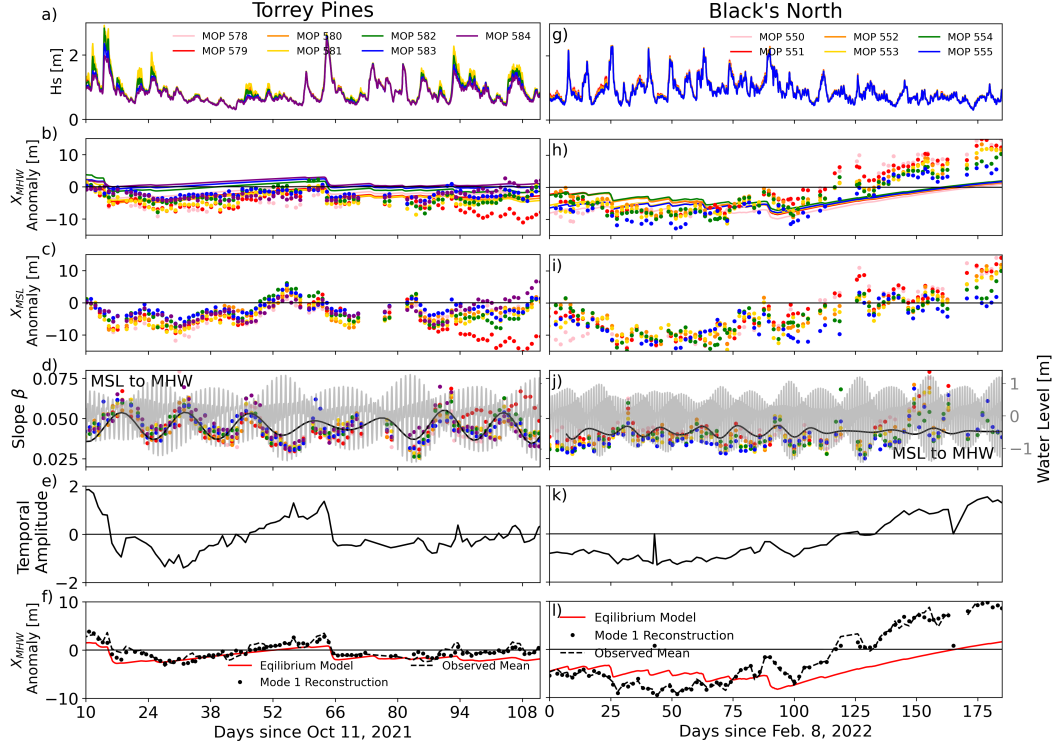


Figure 3. (left) TP: 7 transects surveyed daily for approximately 100 days. (right) BN: 6 transects surveyed every other day for approximately 180 days. Colors (legend) correspond to cross-shore transect line number. Time series of (a,g) significant wave height H_s (m) in 10m depth, (b,h) X_{MHW} anomaly (m, distance of mean high water contour from the mean). Observations (dots) and equilibrium model (curves) are colored by transect (c,i) observed X_{MSL} anomaly (d,j) observed (dots) slope β between X_{MHW} and X_{MSL} . Tide level (grey curves) uses right axis. β is bandpass filtered via complex demodulation at a 14-day period (black solid) to highlight the co-variability with the tide. (e,k) Temporal EOF amplitudes (f,l) X_{MHW} anomaly observed transect mean (dashed line), Mode-1 EOF reconstruction (black dots), and equilibrium model (red line).

153 higher shoreline water levels than X_{MSL} . The optimal datum proxy for volume could
 154 be beach shape and site (including back beach settings) dependent.

155 3 Machine Learning Models

156 Four types of supervised learning methods (linear, support vector, decision trees,
 157 and ensemble regressors) are used to predict X_{MHW} anomaly. These methods use dif-
 158 ferent approaches to identify relationships between input features that minimize a cost
 159 function and optimize the output prediction. While both linear regression and support
 160 vector machine regression identify linear relationships, support vector machine regres-
 161 sion utilizes non-linear kernel transformations to identify such relationships. Learning
 162 methods are implemented with the scikit-learn Python package (Pedregosa et al., 2011).

163 Model predictions, \hat{y} , are evaluated using the coefficient of determination, $r^2 = 1 - \frac{\sum_{i=1}^N (y_i - \hat{y}_i)^2}{\sum_{i=1}^N (y_i - \bar{y})^2}$,

164 and root-mean-square error, $RMSE(y, \hat{y}) = \sqrt{\frac{1}{N} \sum_{i=0}^{N-1} (y_i - \hat{y}_i)^2}$ where y is the ob-
 165 served value, \bar{y} is the sample mean, and N is the number of samples.

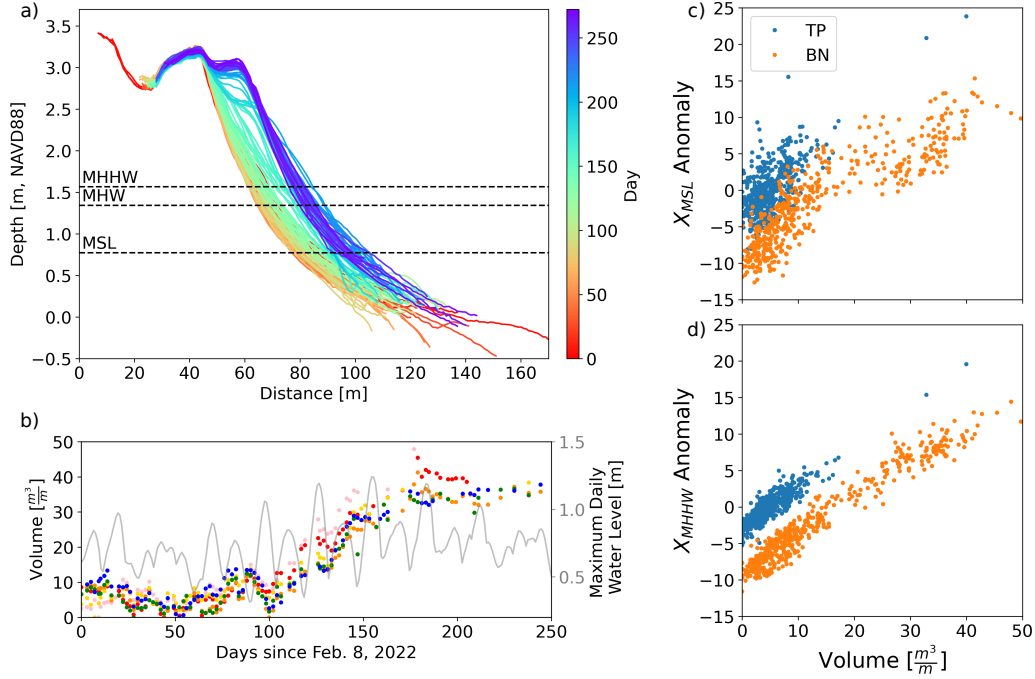


Figure 4. BN (a) subaerial beach elevation (NAVD88) versus distance from back beach origin for 250 days (color bar). (b) Subaerial volume (left axis) and maximum daily tidal water level (right axis) versus time. Colors correspond to MOP number (Figure 4a) (c) X_{MSL} anomaly, and (d) X_{MHWW} anomaly versus beach volume at BN and TP. Dot colors indicate MOP line. For each transect $Vol = \int_{X_{MSL}}^{X_0} Z dx$, where Z is the beach elevation (NAVD88) and $X_0=30\text{m}$ is the cross-shore position where sand elevation change is minimal. At both beaches r^2 is higher for MHHW (TP=0.80, BN=0.95) than MSL (TP=0.45, BN=0.78). MHW (not shown) $r^2 = 0.80, 0.94$, almost identical to MHW.

166

3.1 Linear Regression

167

168

Linear regression model (LR) predictions, \hat{y} , linearly combine p input features, $X=x_{ij}$: $i = 1, 2, \dots, N$, $j = 1, 2, \dots, p$:

$$\hat{y}_i = \beta_0 + \sum_{j=1}^p \beta_j x_{ij} + \epsilon, \quad (1)$$

169

170

where ϵ is the error, β is the coefficient for the input x_{ij} , and β_0 is the trained intercept. The vector β minimizes the residual sum of squares.

171

3.2 Support Vector Machine Regression

172

173

Support Vector Machine regression models (SVM)(Chang & Lin, 2022) use a subset of training data to find a hyperplane, $f(x)$:

$$f(x) = b + \sum_i \alpha_i k(x, x_i), \quad (2)$$

174

that optimizes α_i by minimizing a cost function, C_ϵ :

$$C_\epsilon(y) = \begin{cases} 0, & \text{if } |f(x) - y| < \epsilon_c \\ |f(x) - y| - \epsilon_c, & \text{otherwise,} \end{cases} \quad (3)$$

175 while allowing an error threshold ϵ_c (here 0.1). The input features are transformed into
 176 a higher-dimensional space by a Radial Basis Function (RBF) kernel:

$$k(x, x_i) = e^{-\gamma \|x - x_i\|^2}, \quad (4)$$

177 where γ is $(N * \text{var}(X))^{-1}$, $\text{var}(X)$ is the variance of the input features, X , and $\|x -$
 178 $x_i\|^2$ is the squared distance between data points x and x_i in the original feature space
 179 (Rahimi & Recht, 2007). The transformed data is weighted by the RBF kernel based on
 180 distance between the test point and the data set. Additional kernels were not tested.

181 3.3 Decision Trees and Ensemble Tree Regression

182 Decision trees (DTs) (Breiman et al., 2017) are non-parametric hierarchical model
 183 that use multiple decisions based on trained data to make predictions. The initial node
 184 considers the entire data set. Each subsequent split point, or node, uses a subset of data
 185 determined by preceding branches. Split points are determined to minimize the mean
 186 squared error, $MSE = \frac{1}{n} \sum_{i=1}^n (y_i - \hat{y})^2$.

187 Ensemble methods combine several weak estimators (e.g. DTs) to increase model
 188 accuracy. Gradient Boosting Regressors (GBRs) use data subsets to build regression trees
 189 that minimize errors in previous trees and are trained on a new data subset. Extra Trees
 190 Regressor uses highly randomized trees (Geurts et al., 2006) and data subsets to grow
 191 randomized regression trees with randomly selected split nodes. Each subsequent tree
 192 is fit on the negative gradient of the previous cost function. Model predictions are av-
 193 erages over the 100 (default) regression trees in the forest.

194 3.4 Feature Selection

195 Extra Tree Regression features are motivated by the equilibrium assumption that
 196 beach changes are driven by a disequilibrium between wave energy and bathymetry, with
 197 a time-lagged bathymetry response. Many potential features were explored. The selected
 198 six features are the preceding 12-hr average radiation stress S_{xx} , 30-day and 90-day wave
 199 energy anomaly mean and standard deviation, and previous beach width (Figure 5). Wave
 200 energy anomaly is wave energy minus the 2015 - 2022 mean. Observed, lagged correla-
 201 tions between seasonal shoreline change and time-averaged energy (Miller & Dean, 2007;
 202 Hansen & Barnard, 2010) are reproduced by an equilibrium model (Yates et al., 2011)
 203 so these features are equilibrium compatible but without the simplistic, arbitrary rules
 204 specifying the beach response to disequilibrium.

205 Wave energy anomaly means and standard deviation with 30- and 90-day windows
 206 are highly correlated (Figure 5 and Figure 6, $r^2=0.91$ between 30-day mean and 30-day
 207 standard deviation, and $r^2=0.94$ for the 90-day statistics). These correlations arise be-
 208 cause in southern California, storminess increases both the energy anomaly mean and
 209 standard deviation. Summer waves have low and relatively steady energy. During model
 210 training, the previous beach width is the observed value from the previous survey (Fig-
 211 ure 5b,f black line). In prediction mode, the trained ML model is initialized with a beach
 212 width observation and then steps forward in time using wave time series, similar to the
 213 Equilibrium model (Figure 2,3).

214 No single feature is essential to relatively successful ML performance, as all input
 215 features are highly correlated (or inversely correlated) with beach width (Figure 6). A
 216 subset of any four features has only a small reduction in skill (not shown). More sophis-
 217 ticated methods can be used to reduce feature redundancy.

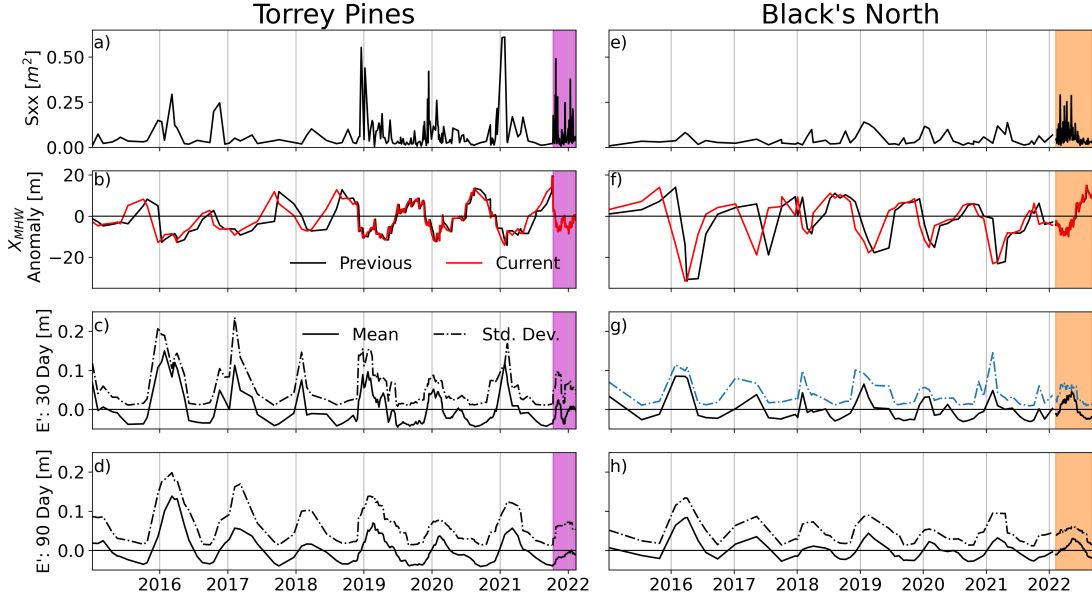


Figure 5. Time series of (a,e) S_{xx} (b,f) previous (black) and current (red) X_{MHW} anomaly (c,g) 30-day and (d,h) 90-day mean (solid) and standard deviation (dashed) of energy anomaly. Features (black) are used to predict current X_{MHW} anomaly (red) during the high frequency prediction period (magenta and orange boxes) at TP (left) and BN (right).

218

3.5 Machine Learning Performance

219

220

221

222

223

224

225

Torrey Pines MOP 581 during high-frequency sampling (Figure 5a-d, magenta box) is used to compare equilibrium and several ML models. The relatively large amount of training data ($N = 185$) includes a year of approximately weekly beach surveys (2019, Figure 2b,c). The trained ML and equilibrium models are assessed as predictive models (Tables 1,2). The input features include time series of wave statistics and an initial beach width. As a model steps forward in time, the previous beach width is updated with the model prediction.

226

227

228

229

230

231

Overall, extra tree (ET) slightly out performs the other supervised learning models with the lowest error (RMSE) and tied for the highest r^2 (Table 1). The Linear Regression model has an equivalent r^2 , but a persistent offset increases the bias and RMSE. Mean absolute error statistics (not shown) are consistent with RMSE. SVM fails to capture the extreme erosion of the initial event (not shown). ET was selected for further comparisons with the equilibrium model.

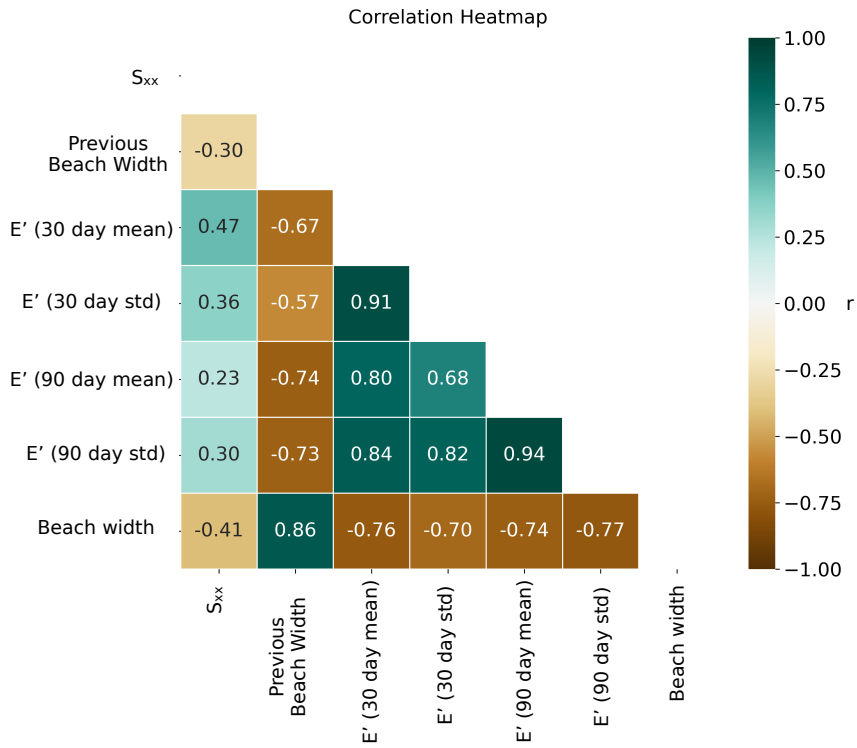


Figure 6. Correlation heat map of input features and beach width. Time series shown in Figure 5.

	RMSE, m	r^2	Bias, m
Linear	3.3	0.63	2.5
Support Vector	2.5	0.46	0.57
Decision Tree	3.0	0.42	0.83
Extra Trees	2.3	0.63	0.85
Gradient Boosting	2.5	0.50	0.35

Table 1. Errors, r^2 , and bias of supervised learning models for TP subweekly sampling.

4 Machine Learning vs. Equilibrium Model

The capabilities of ET and the equilibrium model are compared during two prediction periods. The first prediction is the high-frequency sampling periods at TP and BN (Figure 5, magenta and orange boxes, respectively). Observations from 2015 to the start of high frequency sampling are used for model training. The second prediction period spans the same four years (January 1, 2015 - December 21, 2018) at TP and BN, and observations from Jan 2019 - July 2022 are used for training (Figure 5). At TP the training data includes about one year of approximately weekly sampling.

The equilibrium model does not capture the large (15 m) erosion from the first event of the ‘21/‘22 winter (day 1-3, Figure 7a) and over-predicts erosion during the winter 2015-16 at TP (Figure 7b). These results could not be consistently improved with equilibrium model parameter tuning, but were improved with ML.

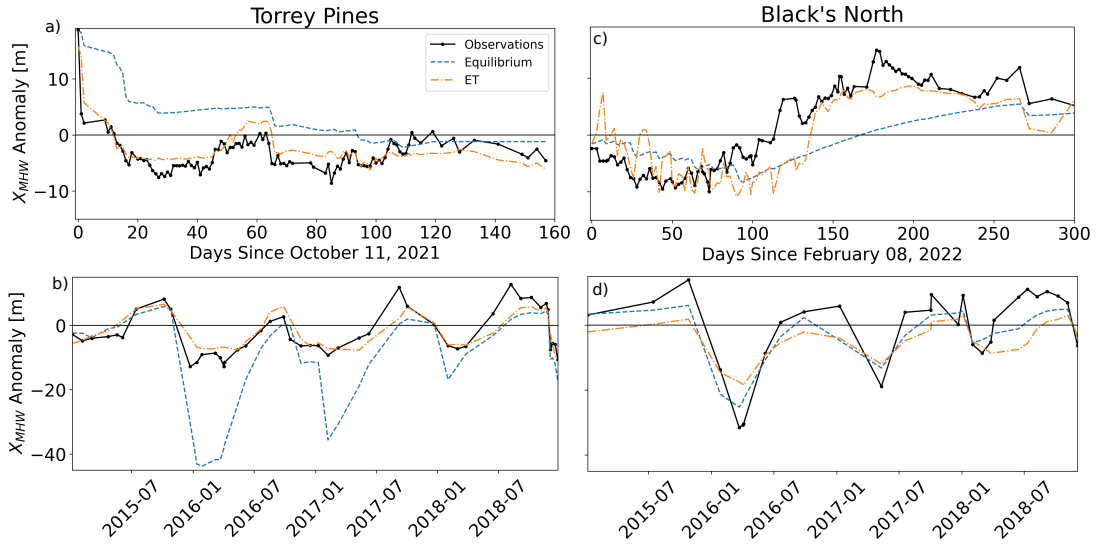


Figure 7. Time series of X_{MHW} anomaly observed (black line with dots) and modeled using the equilibrium model (blue dashed line) and Extra Trees Regressor (ET) model (orange dot-dash curve). (left) TP (MOP 581) and (right) BN (MOP 551). (top) sampled sub-weekly for 160 days at TP and 300 days at BN, and (bottom) roughly monthly for 2015-2018. At both beaches, ET outperforms equilibrium for the sub-weekly observations (Table 2).

At TP, ET outperforms the equilibrium model both during the 6-9 months of sub-weekly sampling and the four years (2015-2018) of less frequent sampling. RMSE with ET is reduced by more than 70% during both periods (Figure 6, Table 2). During the subweekly sampling, ET more accurately predicts the erosion during wave events, particularly during the first wave event (Figure 7a). At Tairua an equilibrium model is also relatively unresponsive to modest wave events that are better captured (Milke Index) by ML methods. However, ML had larger RMSE than equilibrium (table 3 in Gomez-de la Pena et al. (2023)). Furthermore, Equilibrium was tuned for minimum rmse and ML for optimal Milke index, complicating comparisons. At TP, ML clearly outperforms equilibrium independent of the error metric.

At BN, during sub-weekly sampling the ET model also out performs the equilibrium model with a smaller RMSE and larger r^2 (Figure 7c, Table 2). Qualitatively, both the ET and equilibrium models do not accrete as rapidly beginning around day 100; however, around day 140, ET rapidly accretes, reducing the misfit. In contrast to TP, the

258 equilibrium model outperforms ML from 2015-2018, with smaller RMSE and larger r^2
 259 (Table 2). The equilibrium model more closely predict the extreme erosion during the
 260 winter of ‘15-‘16, under predicted by ML by approximately 50%, presumably because
 261 extreme events are lacking in the training period. Qualitatively, ET and equilibrium mod-
 262 els correctly predict the most erosion during winter ‘15-‘16 and least erosion during win-
 263 ter ‘17-‘18. BN illustrates the increased importance of extensive training data to ML per-
 264 formance, relative to the limited training required by equilibrium models (Yates, Guza,
 265 & O’Reilly, 2009) and others .

	Torrey Pines		Black’s North	
	RMSE, m	r^2	RMSE, m	r^2
ET (HF)	2.2	0.63	3.7	0.66
Equilibrium (HF)	7.9	0.22	6.4	0.55
ET (2015-2018)	3.7	0.72	7.4	0.78
Equilibrium (2015-2018)	13.9	0.62	4.9	0.88

Table 2. Error (RMSE) and r^2 of ET and equilibrium models during the high-frequency HF (sub-weekly) test period (3-6 mo, Figure 3) and the 4-year test period (2015-2018).

266 4.1 ML Dependence on Training

267 The sensitivity of the ET model predictions to training data is assessed during the
 268 high-frequency sampling period at TP. Five restrictions to the training dataset are con-
 269 sidered: infrequent (> 30 days) surveys (Figure 8c), approximately weekly surveys for
 270 a limited time span (one year) (Figure 8d), only winter (Figure 8e), and only summer
 271 surveys (Figure 8f). Overall, ML performance is degraded when predictions are based
 272 on less complete training data. The full “all data” training period (Figure 8b) has the
 273 lowest RMSE and highest r^2 (Table 3). Additionally, the “all data” training yields re-
 274 sults most closely resembles the bi-modal shape of the year of sub-weekly observations.
 275 The strong performance of a winter training dataset, which includes a winter of weekly
 276 data, is consistent with the winter prediction period. Using only winter training peri-
 277 ods, ML produces only narrow beaches (Figure 8e), and thus, a negative bias (Table 3).
 278 Alternatively, only summer training data results in a large positive bias, although r^2 is
 only reduced by 20%

	RMSE, m	r^2	Bias
All data	2.3	0.63	0.85
> 30 days	2.8	0.49	1.9
\sim weekly	2.4	0.59	0.74
Only Winter	2.5	0.60	-0.15
Only Summer	4.1	0.50	3.4

Table 3. ET performance when modified training dataset includes only data observed greater than 30 days apart (row 2), only *weekly* data from 2019, during winter only, and during summer only.

280 Despite the limited (one year) time span, the weekly training data performs almost
 281 as well (similar RMSE, low bias and r^2) as the full “all data” training period (Table 3),
 282 highlighting the importance of high frequency training data. The result that 1 year of
 283 training suffices may be specific to TP-like beaches that reach the same annual minimum
 284 beach width due to a non-erodible back beach and/or cobble layer. The more complex
 285 interannual variability at BN presumably requires a wider variety of wave and beach con-
 286 ditions for skillful model training.

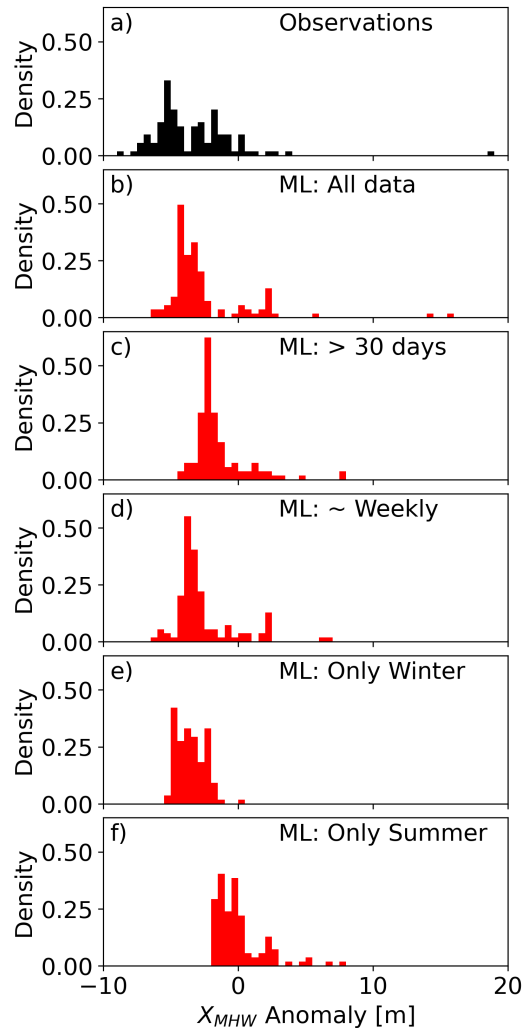


Figure 8. Torrey Pines MOP 581 during the sub-weekly prediction period. Histogram of (a) observations and (b - f) ML predictions trained on different observation subsets. Errors are in Table 3. Densities sum to 1.0 in each panel. ML predictions mirror the properties of the training data.

5 Conclusion

Changes in Mean High Water (MHW) location are tracked at sub-weekly and weekly time scales (Figure 7a,c). A generic equilibrium model replicates observed seasonal variations, but does not account for the cliff and rip rap back beach at TP and over predicts erosion during the 2016 El Niño (Figure 7b). An Extra Tree Regression (ET) model significantly outperforms the equilibrium model (Figure 7). Several (mutually) correlated features characterize the recent wave field (Figure 5), and recent waves are included simplistically as a 12-hr average S_{xx} . Future work includes developing ML estimators using different training features, sub-weekly training data that can resolve the observed 14-day slope variation, and new observations during extreme El Niño conditions.

Appendix A EOF analysis

Empirical orthogonal functions (EOF) decomposes time-space data into orthogonal basis functions that most efficiently captures the total variance. EOF 1 contains about 50 % of the total variance at TP and 93% at BN. EOF-1 is positive across the beach face at both sites, with a maximum $x \sim 70m$ at BN (Figure A1) where the terrace builds over the summer (Figure 4). At TP, the two largest changes in the mode-1 temporal amplitude coincide with narrowing of the beach and large waves with $H_s > 2$ m (Figure 3e). Mode-1 apparently excludes the 14-day tidal signal and provides a less obstructed view of beach evolution from the incident waves alone.

At BN, the temporal amplitude is negative during the winter and spring, when the subaerial beach is eroded, and then increases during summer and fall (Figure 3k). During winter, the equilibrium model and the mode-1 reconstruction show beach erosion response to individual storms (Figure 3l), but the model recovers less than observed.

At TP, significant variance (20%) is contained in mode-2 (Figure A2). Unlike the cross-shore uniform EOF-1, EOF-2 crosses zero between the mean location of MSL and MHW (Figure A2a). The temporal amplitude contains the 14-day tidal signal and fluctuates with the daily max tidal water level (Figure A2b). The mode-2 reconstruction (Figure A2c) shows that sand oscillates with 14-day period between the back and fore beach. During spring tide, sand moves seaward from the back to the fore beach, decreasing the slope. Conversely, during neap tide, sand moves from the fore to the back beach, steepening the beach.

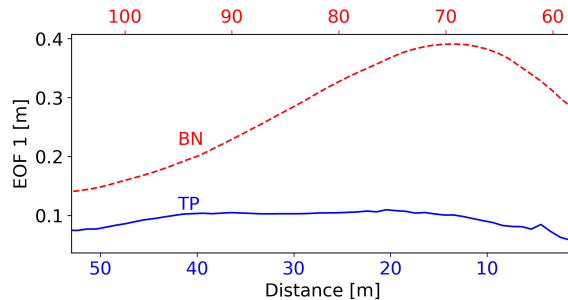


Figure A1. Subaerial EOF Mode-1: Spatial weight versus distance from the back beach origin. TP (blue solid) and BN (red dashed) contain 50% and 93% of the total variance, respectively. Weights are >0 .

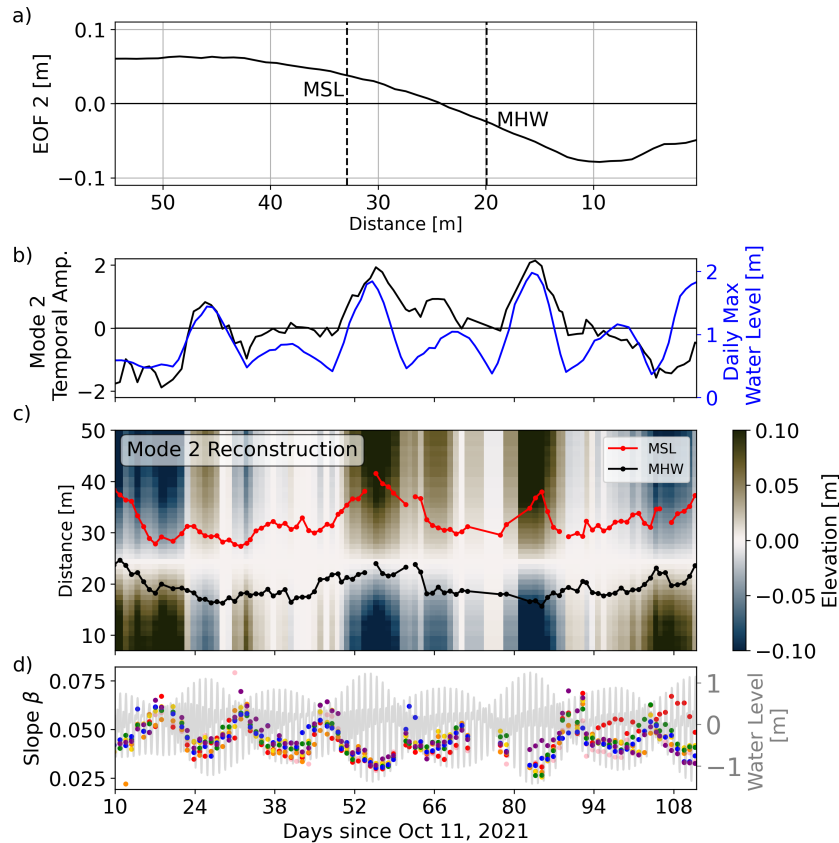


Figure A2. TP EOF Mode-2 contains 20% of the total variance. a) Mode-2 spatial weight versus distance from back beach origin. Spatial weight changes sign between X_{MSL} and X_{MHW} . (b) Mode-2 temporal EOF amplitude (black) and daily maximum water level (blue, right axis) versus time. (c) Mode-2 elevation reconstruction (color bar) versus cross-shore location and time. The distance between X_{MHW} (black) and X_{MSL} (red) contours vary with 14 day period. (d) beach slope β (colored dots correspond to different transects, see Figure 3 legend). Grey curve (right axis) is hourly tidal water level.

318 Open Research Section

319 The data necessary to reproduce results from this paper are currently available through
 320 Google Drive for the purposes of peer review https://drive.google.com/drive/folders/1ozuxQQIDWskc8g8EVNbwrfBmbVTxjg7h?usp=share_link, and will be publicly available
 321 through the University of California, San Diego library digital collections [https://library](https://library.ucsd.edu/dc/)
 322 [.ucsd.edu/dc/](https://library.ucsd.edu/dc/) (doi will be provided upon acceptance). Wave data is available at <https://cdip.ucsd.edu/>
 323

324 Acknowledgments

325 This study was funded by the U.S. Army Corps of Engineers (W912HZ1920020) and the
 326 California Department of Parks and Recreation (C19E0026). Data were collected and
 327 processed by the Coastal Processes Group field team members Lucian Parry, Rob Gren-
 328 zeback, Kent Smith, Brian Woodward, Greg Boyd, Shane Finnerty, Bill Boyd and oth-
 329 ers. Dr. Michele Okihiro organized and coordinated key aspects of the study, including
 330 the approximately 200 high frequency surveys. Thanks to all.

References

- 331
332 Athanasiou, P., van Dongeren, A., Giardino, A., Vousdoukas, M. I., Ranasinghe, R.,
333 & Kwadijk, J. (2020, 12). Uncertainties in projections of sandy beach erosion
334 due to sea level rise: an analysis at the European scale. *Scientific Reports*,
335 *10*(1). doi: 10.1038/s41598-020-68576-0
- 336 Blossier, B., Bryan, K. R., Daly, C. J., & Winter, C. (2017, 10). Shore and bar
337 cross-shore migration, rotation, and breathing processes at an embayed beach.
338 *Journal of Geophysical Research: Earth Surface*, *122*(10), 1745–1770. doi:
339 10.1002/2017JF004227
- 340 Breiman, L., Friedman, J., Olshen, R. A., & Stone, C. J. (2017). *Classification and*
341 *Regression Trees*. CRC Press.
- 342 Chang, C.-C., & Lin, C.-J. (2022, 8). *LIBSVM: A Library for Support Vector Ma-*
343 *chines* (Tech. Rep.). Taipei: National Taiwan University.
- 344 D’Anna, M., Castelle, B., Idier, D., Rohmer, J., Le Cozannet, G., Thieblemont,
345 R., & Bricheno, L. (2021, 8). Uncertainties in Shoreline Projections to 2100
346 at Truc Vert Beach (France): Role of Sea-Level Rise and Equilibrium Model
347 Assumptions. *Journal of Geophysical Research: Earth Surface*, *126*(8). doi:
348 10.1029/2021JF006160
- 349 Davidson, M. A., Splinter, K. D., & Turner, I. L. (2013). A simple equilibrium
350 model for predicting shoreline change. *Coastal Engineering*, *73*, 191–202.
351 Retrieved from [https://www.sciencedirect.com/science/article/pii/](https://www.sciencedirect.com/science/article/pii/S0378383912001676)
352 [S0378383912001676](https://www.sciencedirect.com/science/article/pii/S0378383912001676) doi: <https://doi.org/10.1016/j.coastaleng.2012.11.002>
- 353 Doria, A., Guza, R. T., O’Reilly, W. C., & Yates, M. L. (2016, 8). Observations and
354 modeling of San Diego beaches during El Niño. *Continental Shelf Research*,
355 *124*, 153–164. doi: 10.1016/j.csr.2016.05.008
- 356 Farris, A. S., & List, J. H. (2007, 5). Shoreline change as a proxy for subaerial beach
357 volume change. *Journal of Coastal Research*, *23*(3), 740–748. doi: 10.2112/05
358 -0442.1
- 359 Geurts, P., Ernst, D., & Wehenkel, L. (2006, 4). Extremely randomized trees. *Ma-*
360 *chine Learning*, *63*(1), 3–42. doi: 10.1007/s10994-006-6226-1
- 361 Gomez-de la Pena, E., Coco, G., Whittaker, C., & Montano, J. (2023). On the
362 use of Convolutional Deep Learning to predict shoreline change. *EGUsphere*
363 *[preprint]*, *2023*, 1–24. Retrieved from [https://egusphere.copernicus.org/](https://egusphere.copernicus.org/preprints/2023/egusphere-2023-958/)
364 [preprints/2023/egusphere-2023-958/](https://egusphere.copernicus.org/preprints/2023/egusphere-2023-958/) doi: 10.5194/egusphere-2023-958
- 365 Hansen, J. E., & Barnard, P. L. (2010, 11). Sub-weekly to interannual variability
366 of a high-energy shoreline. *Coastal Engineering*, *57*(11-12), 959–972. doi: 10
367 .1016/j.coastaleng.2010.05.011
- 368 Harley, M. D., Turner, I. L., Short, A. D., & Ranasinghe, R. (2011, 12). A reeval-
369 uation of coastal embayment rotation: The dominance of cross-shore versus
370 alongshore sediment transport processes, Collaroy-Narrabeen Beach, south-
371 east Australia. *Journal of Geophysical Research: Earth Surface*, *116*(4). doi:
372 10.1029/2011JF001989
- 373 Henderson, C. S., Fiedler, J. W., Merrifield, M. A., Guza, R. T., & Young, A. P.
374 (2022, 8). Phase resolving runup and overtopping field validation of SWASH.
375 *Coastal Engineering*, *175*. doi: 10.1016/j.coastaleng.2022.104128
- 376 Kalligeris, N., Smit, P. B., Ludka, B. C., Guza, R. T., & Gallien, T. W. (2020,
377 6). Calibration and assessment of process-based numerical models for beach
378 profile evolution in southern California. *Coastal Engineering*, *158*. doi:
379 10.1016/j.coastaleng.2020.103650
- 380 Ludka, B. C., Guza, R. T., O’Reilly, W. C., & Yates, M. L. (2015). Field evi-
381 dence of beach profile evolution toward equilibrium. *Journal of Geophys-*
382 *ical Research: Oceans*, *120*(11), 7574–7597. Retrieved from [https://](https://agupubs.onlinelibrary.wiley.com/doi/abs/10.1002/2015JC010893)
383 agupubs.onlinelibrary.wiley.com/doi/abs/10.1002/2015JC010893 doi:
384 <https://doi.org/10.1002/2015JC010893>
- 385 Matsumoto, H., & Young, A. P. (2022, 12). Quantitative regional observations of

- 386 gravel and bedrock influence on beach morphologies. *Geomorphology*, 419. doi:
387 10.1016/j.geomorph.2022.108491
- 388 Matsumoto, H., Young, A. P., & Guza, R. T. (2020). Cusp and Mega Cusp
389 Observations on a Mixed Sediment Beach. Retrieved from [https://](https://agupubs.onlinelibrary.wiley.com/doi/10.1029/2020EA001366)
390 agupubs.onlinelibrary.wiley.com/doi/10.1029/2020EA001366 doi:
391 10.1029/2020EA001366-T
- 392 Miller, J. K., & Dean, R. G. (2004). A simple new shoreline change model. *Coastal*
393 *Engineering*, 51(7), 531–556. Retrieved from [https://www.sciencedirect](https://www.sciencedirect.com/science/article/pii/S0378383904000614)
394 [.com/science/article/pii/S0378383904000614](https://www.sciencedirect.com/science/article/pii/S0378383904000614) doi: [https://doi.org/](https://doi.org/10.1016/j.coastaleng.2004.05.006)
395 10.1016/j.coastaleng.2004.05.006
- 396 Miller, J. K., & Dean, R. G. (2007, 2). Shoreline variability via empirical orthogo-
397 nal function analysis: Part II relationship to nearshore conditions. *Coastal En-*
398 *gineering*, 54(2), 133–150. doi: 10.1016/j.coastaleng.2006.08.014
- 399 Montaña, J., Coco, G., Antolínez, J. A., Beuzen, T., Bryan, K. R., Cagigal, L., ...
400 Vos, K. (2020, 12). Blind testing of shoreline evolution models. *Scientific*
401 *Reports*, 10(1). doi: 10.1038/s41598-020-59018-y
- 402 Muñoz-Pérez, J. J., & Medina, R. (2000). *Profile Changes due to a Fortnightly Tidal*
403 *Cycle* (Tech. Rep.).
- 404 O'Reilly, W. C., Olfe, C. B., Thomas, J., Seymour, R. J., & Guza, R. T. (2016).
405 The California coastal wave monitoring and prediction system. *Coastal En-*
406 *gineering*, 116, 118–132. Retrieved from [https://www.sciencedirect.com/](https://www.sciencedirect.com/science/article/pii/S0378383916301120)
407 [science/article/pii/S0378383916301120](https://www.sciencedirect.com/science/article/pii/S0378383916301120) doi: [https://doi.org/10.1016/](https://doi.org/10.1016/j.coastaleng.2016.06.005)
408 [j.coastaleng.2016.06.005](https://doi.org/10.1016/j.coastaleng.2016.06.005)
- 409 Pedregosa, F., Michel, V., Grisel, O., Blondel, M., Prettenhofer, P., Weiss, R.,
410 ... Duchesnay, (2011). Scikit-learn: Machine Learning in Python.
411 *Journal of Machine Learning Research*, 12, 2825–2830. Retrieved from
412 <http://scikit-learn.sourceforge.net>.
- 413 Phillips, M. S., Harley, M. D., Turner, I. L., Splinter, K. D., & Cox, R. J. (2017,
414 3). Shoreline recovery on wave-dominated sandy coastlines: the role of sand-
415 bar morphodynamics and nearshore wave parameters. *Marine Geology*, 385,
416 146–159. doi: 10.1016/j.margeo.2017.01.005
- 417 Rahimi, A., & Recht, B. (2007). Random Features for Large-Scale Kernel Machines.
418 In J. Platt, D. Koller, Y. Singer, & S. Roweis (Eds.), *Advances in neural in-*
419 *formation processing systems* (Vol. 20). Curran Associates, Inc. Retrieved
420 from [https://proceedings.neurips.cc/paper_files/paper/2007/file/](https://proceedings.neurips.cc/paper_files/paper/2007/file/013a006f03dbc5392effeb8f18fda755-Paper.pdf)
421 [013a006f03dbc5392effeb8f18fda755-Paper.pdf](https://proceedings.neurips.cc/paper_files/paper/2007/file/013a006f03dbc5392effeb8f18fda755-Paper.pdf)
- 422 Ruggerio, P., Kratzmann, M. G., Himmelstoss, E. A., Reid, D., Allan, J., & Kamin-
423 sky, G. (2013). *National assessment of shoreline change: historical shoreline*
424 *change along the Pacific Northwest coast* (Tech. Rep.). Reston, VA. Re-
425 trieved from <http://pubs.er.usgs.gov/publication/ofr20121007> doi:
426 10.3133/ofr20121007
- 427 Ruggiero, P., Buijsman, M., Kaminsky, G. M., & Gelfenbaum, G. (2010). Model-
428 ing the effects of wave climate and sediment supply variability on large-scale
429 shoreline change. *Marine Geology*, 273(1), 127–140. Retrieved from [https://](https://www.sciencedirect.com/science/article/pii/S0025322710000708)
430 www.sciencedirect.com/science/article/pii/S0025322710000708 doi:
431 <https://doi.org/10.1016/j.margeo.2010.02.008>
- 432 Sallenger, A. H., Krabill, W., Brock, J., Swift, R., Manizade, S., & Stockdon,
433 H. (2002). *Sea-cliff erosion as a function of beach changes and extreme*
434 *wave runup during the 1997-1998 El Niño* (Tech. Rep.). Retrieved from
435 www.elsevier.com/locate/margeo
- 436 Simmons, J. A., & Splinter, K. D. (2022, 4). A multi-model ensemble approach to
437 coastal storm erosion prediction. *Environmental Modelling and Software*, 150.
438 doi: 10.1016/j.envsoft.2022.105356
- 439 Splinter, K. D., Turner, I. L., Davidson, M. A., Barnard, P., Castelle, B., &
440 Oltman-Shay, J. (2014). A generalized equilibrium model for predict-

- 441 ing daily to interannual shoreline response. *Journal of Geophysical Re-*
442 *search: Earth Surface*, 119(9), 1936–1958. Retrieved from [https://](https://agupubs.onlinelibrary.wiley.com/doi/abs/10.1002/2014JF003106)
443 agupubs.onlinelibrary.wiley.com/doi/abs/10.1002/2014JF003106 doi:
444 <https://doi.org/10.1002/2014JF003106>
- 445 Straub, J. A., Rodriguez, A. B., Luettich, R. A., Moore, L. J., Itzkin, M., Ridge,
446 J. T., ... Theuerkauf, E. J. (2020, 7). The role of beach state and the timing
447 of pre-storm surveys in determining the accuracy of storm impact assessments.
448 *Marine Geology*, 425. doi: 10.1016/j.margeo.2020.106201
- 449 Wright, L. D., Short, A. D., & Green, M. O. (1985). Short-term changes in
450 the morphodynamic states of beaches and surf zones: An empirical predic-
451 tive model. *Marine Geology*, 62(3), 339–364. Retrieved from [https://](https://www.sciencedirect.com/science/article/pii/0025322785901239)
452 www.sciencedirect.com/science/article/pii/0025322785901239 doi:
453 [https://doi.org/10.1016/0025-3227\(85\)90123-9](https://doi.org/10.1016/0025-3227(85)90123-9)
- 454 Yates, M. L., Guza, R. T., & O'Reilly, W. C. (2009). Equilibrium shoreline re-
455 sponse: Observations and modeling. *Journal of Geophysical Research: Oceans*,
456 114(C9). Retrieved from [https://agupubs.onlinelibrary.wiley.com/doi/](https://agupubs.onlinelibrary.wiley.com/doi/abs/10.1029/2009JC005359)
457 [abs/10.1029/2009JC005359](https://agupubs.onlinelibrary.wiley.com/doi/abs/10.1029/2009JC005359) doi: <https://doi.org/10.1029/2009JC005359>
- 458 Yates, M. L., Guza, R. T., O'Reilly, W. C., Hansen, J. E., & Barnard, P. L. (2011).
459 Equilibrium shoreline response of a high wave energy beach. *Journal of Geo-*
460 *physical Research: Oceans*, 116(4). doi: 10.1029/2010JC006681
- 461 Yates, M. L., Guza, R. T., O'Reilly, W. C., & Seymour, R. J. (2009). Overview of
462 seasonal sand level changes on southern California Beaches. *Shore & Beaches*,
463 77(1), 39–46.

Subaerial Profiles at Two Beaches: Equilibrium and Machine Learning

M. N. Siegelman¹, R. A. McCarthy¹, A. P. Young¹, W. O'Reilly¹, H. Matsumoto¹, M. Johnson¹, C. Mack¹, and R. T. Guza¹

¹Scripps Institution of Oceanography, 9500 Gilman Drive, La Jolla, CA 92037 USA

Key Points:

- At two beaches, weekly to quarterly elevation surveys spanning 700-800 m along-shore and 8 years were supplemented with ~ 100 subweekly surveys spanning several months.
- The Equilibrium-informed Extra Tree (ET) Regression Machine Learning model uses features (e.g. 30 day wave energy anomaly) inspired by equilibrium concepts
- With sufficient training, ET outperforms a generic equilibrium model

Corresponding author: Mika N. Siegelman, msiegelman@ucsd.edu

Abstract

Weekly to quarterly beach elevation surveys spanning 700-800 m alongshore and 8 years at two beaches were each supplemented with several months of ~ 100 sub-weekly surveys. These beaches, which have different sediment types (sand vs. sand-cobble mix), both widen in summer in response to the seasonal wave climate, in agreement with a generic equilibrium model. Results suggest differences in backshore erodability contribute to differing beach responses in the stormiest (El Niño) year. At both sites, the time dependence of the equilibrium modeled shoreline resembles the first mode of an EOF decomposition of the observations. With sufficient training, an equilibrium-informed Extra Tree Regression model, that includes features motivated by equilibrium modelling, can significantly outperform a generic equilibrium model.

Plain Language Summary

Beach elevation surveys are compared at two beaches in San Diego County. Both beaches narrow during winter as large wave events transport sand offshore and widen during summer as gentle waves move sand onshore. The seasonality of such beaches has been characterized by simple models that primarily rely on wave energy relative to an average state to predict beach width changes, known as equilibrium models. Here, we highlight some of the limitations of equilibrium models, such as a tendency to over predict winter erosion at a beach backed by non-erodible infrastructure. We demonstrate that machine learning models, when trained with sufficient observations, can predict beach width changes more accurately than equilibrium models.

1 Introduction

Forecasting wave runup and overtopping depends on reliable estimates of future waves and nearshore bathymetry. Wave model forecasts are increasingly accurate on time scales ranging from several days to seasons. However, changes in beach bathymetry (e.g. shoreline location and beach slope) are understood poorly. Many authors emphasize the feedback between runup and evolving bathymetry, and the relative lack of comprehensive (in space and time) bathymetry observations for model validation (e.g. Straub et al. (2020); Henderson et al. (2022) and many others).

Using standardized calibration and test periods, Montaña et al. (2020) compared the performance of 12 “Equilibrium” and 7 ML models with designated calibration and testing periods at Tairua Beach in New Zealand. As a comparison baseline for errors, the data were detrended with no further adjustment. RMSE (root-mean-square-error) was never reduced by more than 20% from the baseline RMSE ≈ 5.3 m, and in most cases the error reduction was $< 10\%$ (Figure 3 in Montaña et al. (2020)). Overall, Equilibrium and ML models performed similarly with low skill. Blossier et al. (2017) report shoreline location errors at Tairua between +3.50 m and -4 m, suggesting that noise could have limited model skill. More recently, Gomez-de la Pena et al. (2023) compared Tairua observations with model results using complex neural network (CNN), hybrid CNN-LSTM, and equilibrium models. LSTMs extract sequential information and long-term temporal dependencies. Shoreline evolution is strongly seasonal, so the hybrid Gomez-de la Pena et al. (2023) model would be expected to outperform the memory-lacking CNN; however, CNN and hybrid models yielded similar RMSE. Gomez-de la Pena et al. (2023) review some of rapidly expanding applications of ML to shoreline change.

Process-based models, such as XBeach, Cshore, SBeach, and COAWST, often show skill in simulating erosion from individual storms when tuned with site-specific observations, but optimal parameter values can vary (unpredictably) in space and time (Kalligeris et al., 2020). Recovery is not reliably modeled, errors accumulate in long-term simulations, and process-based models have not been successfully used for years-long simula-

tions. Storm erosion is more accurately simulated with a neural network than with SBeach or XBeach (Simmons & Splinter, 2022).

Equilibrium beach models, noteworthy for their numerical simplicity and relatively few free parameters, quantify the hypotheses (Wright et al., 1985; Miller & Dean, 2004) that for a constant wave field there is an equilibrium beach morphology (the equilibrium beach) that would remain constant in time, neither eroding nor accreting. A beach in disequilibrium with ambient waves changes towards the equilibrium shape at a rate proportional to the disequilibrium: $\frac{dX_{MHW}}{dt} = C^\pm E^{1/2} \Delta E$, where E is wave energy, and C^\pm are change rate coefficients. The energy disequilibrium, ΔE , is the difference between the wave energy and an equilibrium energy, $E_{eq}(X_{MHW}) = aX_{MHW} + b$, where a and b are fit to observations. The functional forms for $\frac{dX_{MHW}}{dt}$ and $E_{eq}(X_{MHW})$ are somewhat arbitrary and many variants of these forms have similar skill (Yates, Guza, & O’Reilly, 2009; Davidson et al., 2013).

When calibrated with observed waves and shoreline locations, equilibrium models qualitatively reproduce shoreline change on seasonal to interannual time scales (Miller & Dean, 2004; Yates, Guza, & O’Reilly, 2009; Ruggiero et al., 2010; Davidson et al., 2013; Ruggiero et al., 2013; Splinter et al., 2014; Ludka et al., 2015). Equilibrium models are often used to simulate beach response to climate change (e.g. sea level rise) because of their simplicity (Athanasίου et al., 2020; D’Anna et al., 2021) and lack of viable alternatives. Equilibrium models and ML are both data-driven. Equilibrium models make sweeping assumptions that reduce the model complexity to a few (between 2 and 4) constants in a first order differential equation. ML (as used here) is relatively assumption free and allows unlimited model complexity.

In Section 2, we describe about 8 years of seasonal beach elevation surveys supplemented with ~ 100 sub-weekly surveys spanning several months. Seasonal changes are reproduced relatively well with an equilibrium model, but sub-weekly observations are not. ML models are presented in section 3, and compared with observations and equilibrium in section 4. Results are discussed in Section 5.

2 Study Site

Sand level observations span almost 8 years (2015-2022) and 600 m at Torrey Pines State Beach (TP) and 500 m at north Black’s Beach (BN), separated by approximately 2.4 km (Figures 1 and 2). Wave buoys and models are used to hindcast and forecast hourly waves on transects spaced 100 m, known as MOP lines (O’Reilly et al., 2016). TP contains 7 MOP lines (578-584) and BN contains 6 (MOP 550-555) (Figure 1 and 2). During winter storms, the significant wave height, H_s , can reach ~ 4 m at both sites (Figure 2a,d). The spring tidal range is ~ 2 m.

2.1 Subaerial Sand Elevation

Subaerial beach surveys before 2017 were approximately quarterly with an ATV mounted RTK GPS. Beginning in 2017, surveys collected with a truck mounted LiDAR (RIEGL VMZ-2000 laser scanner) are gridded (1 m x 1 m) after removing the swash zone, ground filtering, and manual noise removal. TP was usually surveyed on timescales ranging from weekly to monthly but was surveyed weekly for the entirety of 2019. BN LiDAR surveys were usually quarterly with some monthly surveys (Figure 2, Matsumoto and Young (2022)).

A cart mounted RTK GPS system surveyed along MOP transects from the back beach to a target minimum elevation of 0.774 m (NAVD88, MSL) during high frequency sampling (colored boxes in Figure 2), even when tides and waves were not low and the survey area was in the inner surf zone (Figures 3 and 4). Daily TP (578-584) surveys spanned

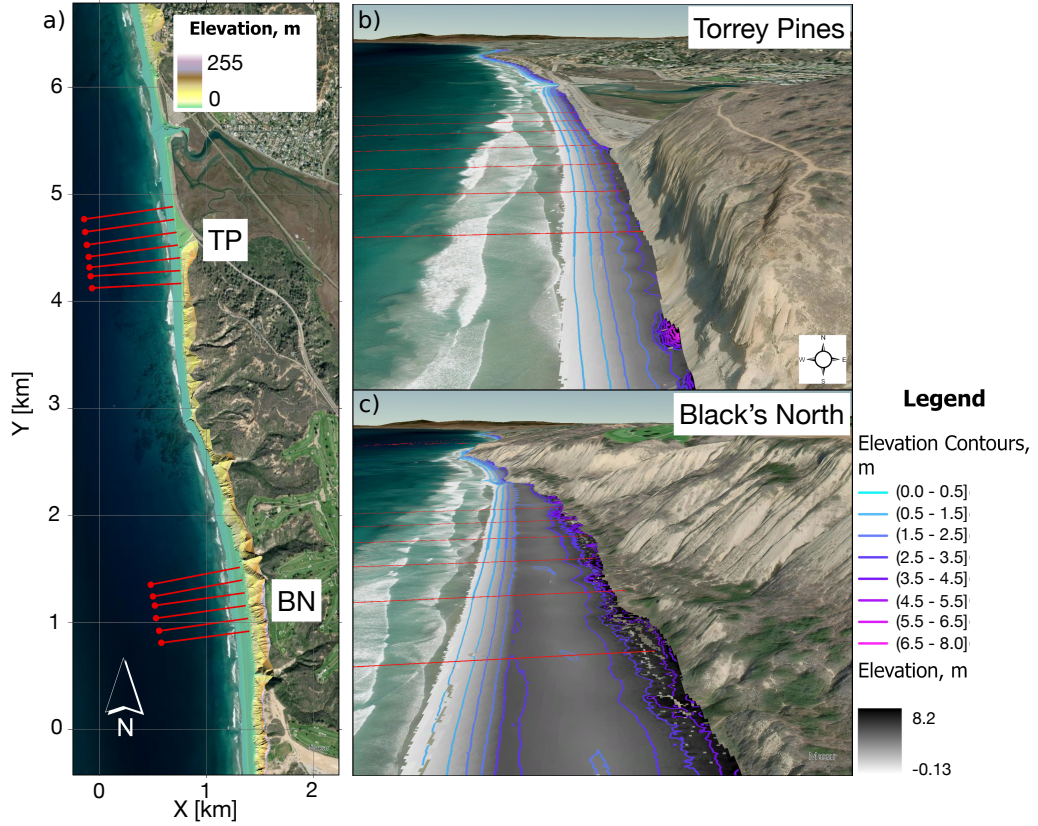


Figure 1. a) Torrey Pines (TP) and Black's North (BN) locations and (b,c) aerial photos. Cross-shore transects (solid red lines) are spaced 100 m alongshore. Elevation contours (legend) show a wide terrace at BN. Steep cliffs and riprap back the narrower TP, where beach cusps appear as alongshore periodic purple mounds at the cliff base and the 2.5-3.5 m contour location.

110 110 days from October 11, 2021 – February 3, 2022, with approximately a one week De-
 111 cember gap. BN (550-555) was surveyed every other day for 180 days from February 8,
 112 2022 – July 21, 2022 (Figure 3).

113 Free parameter values of Yates, Guza, and O'Reilly (2009), tuned at TP, are used
 114 here for both TP and BN. We use X_{MHW} rather than X_{MSL} (Yates, Guza, & O'Reilly,
 115 2009) because beach volume is better correlated with X_{MHW} than X_{MSL} (Section 2.2).
 116 Re-tuning model parameter values does not significantly improve model skill.

117 Southern California waves are relatively energetic during winter and calm during
 118 summer (Figure 2a,d). Both beaches widen during summer and narrow during winter,
 119 in agreement with a generic equilibrium model (Yates, Guza, and O'Reilly (2009), Fig-
 120 ure 2b,e, blue line). During summer, both beaches are primarily sandy (median diam-
 121 eter 0.25 mm (Yates, Guza, O'Reilly, & Seymour, 2009)). At TP, winter erosion often
 122 exposes cobble, sometimes as extensive cobble berms and cusps. (Matsumoto et al., 2020).

123 Shoreline responses in the stormiest year ('15/'16 El Niño, Figure 2, green arrows)
 124 differ. At TP, X_{MHW} plateaus at about the same location every winter, regardless of
 125 wave conditions. Doria et al. (2016) attributes the plateau to "erosion resistant bound-
 126 aries," including cliffs or rip rap and the cobble layer, which become exposed during the
 127 winter. In contrast, BN is backed by an erodible sand berm (Figure 4). A generic equi-
 128 librium lacks the complexity to include such details.

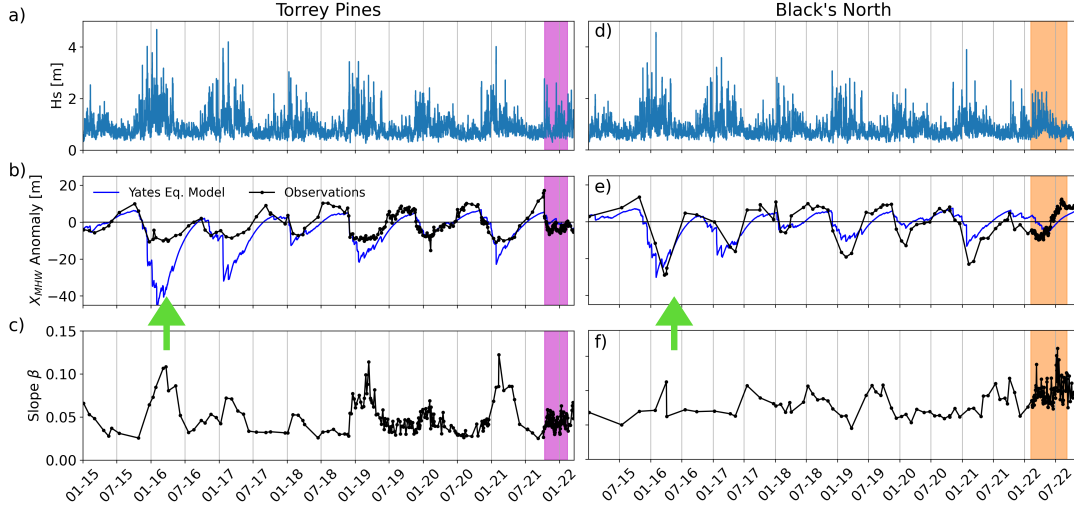


Figure 2. Left (Torrey Pines), right (Black's North) time series (almost 8 years) (a,d) significant wave height, H_s , in 10 m depth, (b,e) X_{MHW} anomaly (the cross-shore distance between the MHW contour and the mean (averaged over time and MOP lines at each beach). Equilibrium model (blue curve) uses constants (except for the mean shoreline location) from (Yates, Guza, & O'Reilly, 2009). Arrows mark 2016 winter when the BN sandy back beach retreated more than at cliff-backed TP. (c,f) slope, β , between MHW and MSL contours. Sub-weekly observations (vertical color bars) are detailed in Figure 3.

129 Despite the overall similar seasonal response of beach width to the wave conditions,
 130 the beach slope, β , (defined between X_{MSL} and X_{MHW}) response is opposite at BN and
 131 TP (Figure 2c,f). At TP, the summer, accreted profile has a gentle slope, whereas in BN's
 132 most accreted state, a prominent, steep-faced terrace forms between 50 m and 100 m from
 133 the back beach during the summer and spring. As the terrace erodes, the beach face re-
 134 retreats and the slope decreases.

135 During daily sampling at TP, two events with $H_s > 2.5$ m caused limited beach
 136 narrowing, consistent with an equilibrium model (days 12 and 60, Figure 3a). Between
 137 wave events, the observed and modeled beach weakly accrete. As winter continues (day
 138 80), the spread between MOP transects at TP increases possibly owing to composite sand-
 139 cobble cusps and megacusps. A similar pattern of increasing alongshore complexity over
 140 the course of the winter is observed with the weekly truck LiDAR (Matsumoto et al.,
 141 2020). The slope (between X_{MSL} and X_{MHW}) varied seasonally, but also with 14-day
 142 (spring-neap) period (Figure 3d,j) (Muñoz-Pérez & Medina, 2000; Phillips et al., 2017).
 143 Temporal EOF amplitudes of the observed X_{MHW} anomaly, Mode-1 EOF reconstruction,
 144 and equilibrium model are similar (Figure 3f,l). EOFs are discussed in Appendix
 145 A.

146 2.2 Subaerial Volume and Proxies

147 Historically, X_{MSL} , X_{MHW} and X_{MHHW} have all been used as shoreline reference
 148 contours for beach width (Sallenger et al., 2002; Farris & List, 2007; Yates, Guza, O'Reilly,
 149 & Seymour, 2009; Harley et al., 2011). Here, subaerial volumes, Vol , at BN and TP are
 150 more highly correlated with X_{MHW} and X_{MHHW} than with X_{MSL} (Figure 4c,d). X_{MHW}
 151 is used below (e.g. Figure 7) X_{MSL} is relatively unresponsive to volume changes high
 152 on the accreted profile. Furthermore, subaerial surveys of X_{MHW} can be measured with

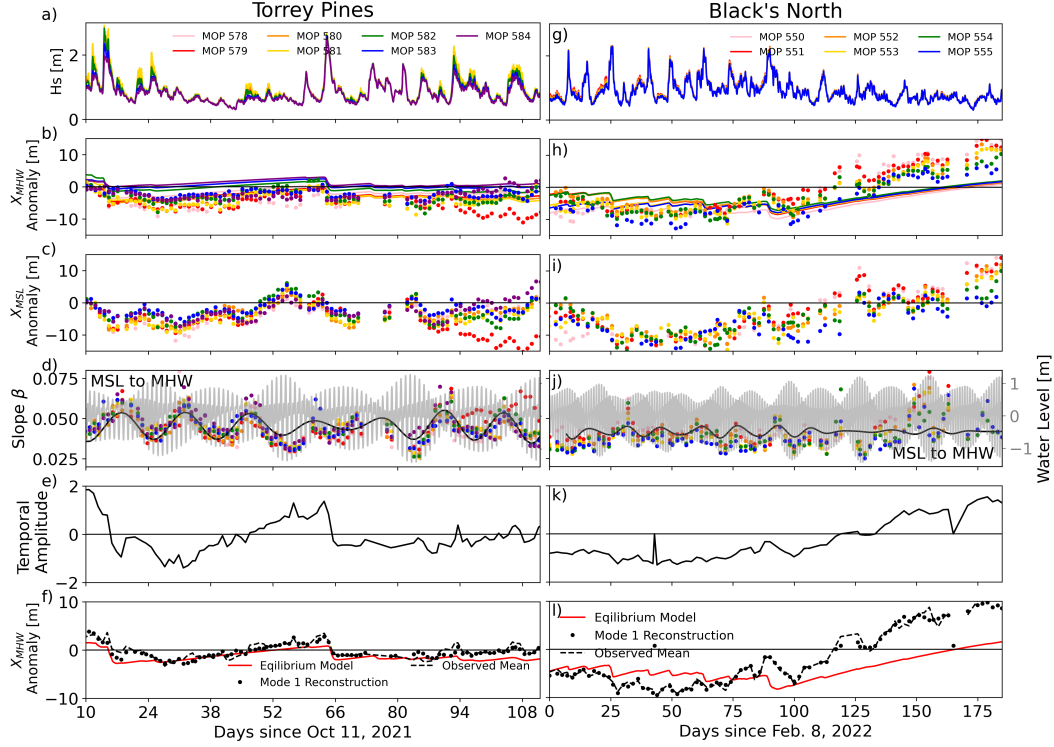


Figure 3. (left) TP: 7 transects surveyed daily for approximately 100 days. (right) BN: 6 transects surveyed every other day for approximately 180 days. Colors (legend) correspond to cross-shore transect line number. Time series of (a,g) significant wave height H_s (m) in 10m depth, (b,h) X_{MHW} anomaly (m, distance of mean high water contour from the mean). Observations (dots) and equilibrium model (curves) are colored by transect (c,i) observed X_{MSL} anomaly (d,j) observed (dots) slope β between X_{MHW} and X_{MSL} . Tide level (grey curves) uses right axis. β is bandpass filtered via complex demodulation at a 14-day period (black solid) to highlight the co-variability with the tide. (e,k) Temporal EOF amplitudes (f,l) X_{MHW} anomaly observed transect mean (dashed line), Mode-1 EOF reconstruction (black dots), and equilibrium model (red line).

153 higher shoreline water levels than X_{MSL} . The optimal datum proxy for volume could
 154 be beach shape and site (including back beach settings) dependent.

155 3 Machine Learning Models

156 Four types of supervised learning methods (linear, support vector, decision trees,
 157 and ensemble regressors) are used to predict X_{MHW} anomaly. These methods use dif-
 158 ferent approaches to identify relationships between input features that minimize a cost
 159 function and optimize the output prediction. While both linear regression and support
 160 vector machine regression identify linear relationships, support vector machine regres-
 161 sion utilizes non-linear kernel transformations to identify such relationships. Learning
 162 methods are implemented with the scikit-learn Python package (Pedregosa et al., 2011).

163 Model predictions, \hat{y} , are evaluated using the coefficient of determination, $r^2 = 1 - \frac{\sum_{i=1}^N (y_i - \hat{y}_i)^2}{\sum_{i=1}^N (y_i - \bar{y})^2}$,

164 and root-mean-square error, $RMSE(y, \hat{y}) = \sqrt{\frac{1}{N} \sum_{i=0}^{N-1} (y_i - \hat{y}_i)^2}$ where y is the ob-
 165 served value, \bar{y} is the sample mean, and N is the number of samples.

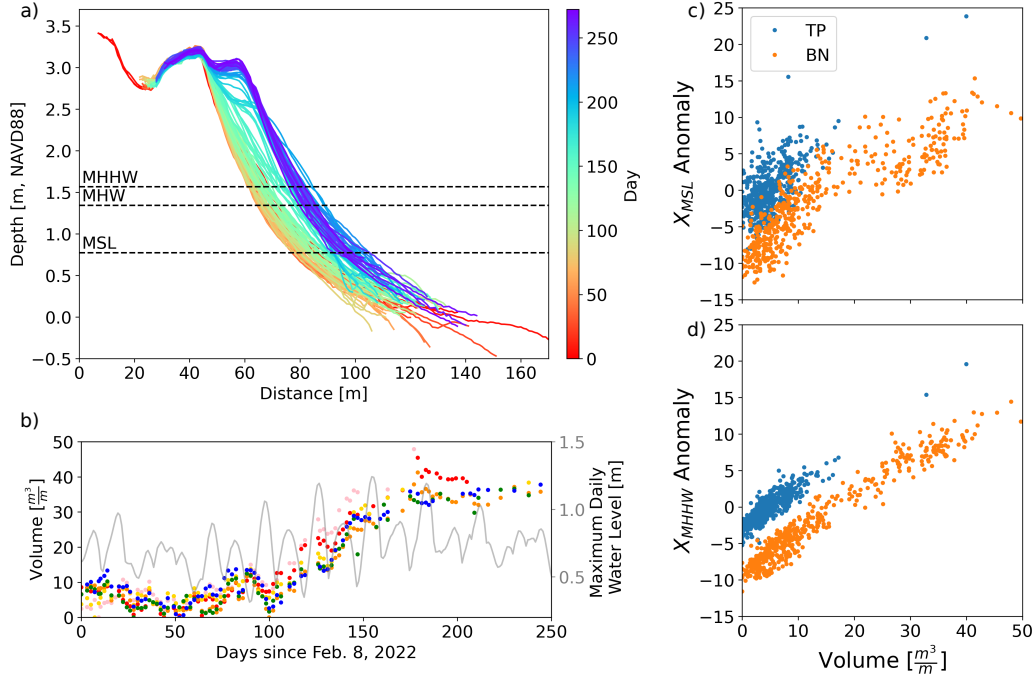


Figure 4. BN (a) subaerial beach elevation (NAVD88) versus distance from back beach origin for 250 days (color bar). (b) Subaerial volume (left axis) and maximum daily tidal water level (right axis) versus time. Colors correspond to MOP number (Figure 4a) (c) X_{MSL} anomaly, and (d) X_{MHWW} anomaly versus beach volume at BN and TP. Dot colors indicate MOP line. For each transect $Vol = \int_{X_{MSL}}^{X_0} Z dx$, where Z is the beach elevation (NAVD88) and $X_0=30m$ is the cross-shore position where sand elevation change is minimal. At both beaches r^2 is higher for MHHW (TP=0.80, BN=0.95) than MSL (TP=0.45, BN=0.78). MHW (not shown) $r^2 = 0.80, 0.94$, almost identical to MHW.

166

3.1 Linear Regression

167

168

Linear regression model (LR) predictions, \hat{y} , linearly combine p input features, $X=x_{ij}$: $i = 1, 2, \dots, N$, $j = 1, 2, \dots, p$:

$$\hat{y}_i = \beta_0 + \sum_{j=1}^p \beta_j x_{ij} + \epsilon, \quad (1)$$

169

170

where ϵ is the error, β is the coefficient for the input x_{ij} , and β_0 is the trained intercept. The vector β minimizes the residual sum of squares.

171

3.2 Support Vector Machine Regression

172

173

Support Vector Machine regression models (SVM)(Chang & Lin, 2022) use a subset of training data to find a hyperplane, $f(x)$:

$$f(x) = b + \sum_i \alpha_i k(x, x_i), \quad (2)$$

174

that optimizes α_i by minimizing a cost function, C_ϵ :

$$C_\epsilon(y) = \begin{cases} 0, & \text{if } |f(x) - y| < \epsilon_c \\ |f(x) - y| - \epsilon_c, & \text{otherwise,} \end{cases} \quad (3)$$

175 while allowing an error threshold ϵ_c (here 0.1). The input features are transformed into
 176 a higher-dimensional space by a Radial Basis Function (RBF) kernel:

$$k(x, x_i) = e^{-\gamma \|x - x_i\|^2}, \quad (4)$$

177 where γ is $(N * \text{var}(X))^{-1}$, $\text{var}(X)$ is the variance of the input features, X , and $\|x -$
 178 $x_i\|^2$ is the squared distance between data points x and x_i in the original feature space
 179 (Rahimi & Recht, 2007). The transformed data is weighted by the RBF kernel based on
 180 distance between the test point and the data set. Additional kernels were not tested.

181 3.3 Decision Trees and Ensemble Tree Regression

182 Decision trees (DTs) (Breiman et al., 2017) are non-parametric hierarchical model
 183 that use multiple decisions based on trained data to make predictions. The initial node
 184 considers the entire data set. Each subsequent split point, or node, uses a subset of data
 185 determined by preceding branches. Split points are determined to minimize the mean
 186 squared error, $MSE = \frac{1}{n} \sum_{i=1}^n (y_i - \hat{y})^2$.

187 Ensemble methods combine several weak estimators (e.g. DTs) to increase model
 188 accuracy. Gradient Boosting Regressors (GBRs) use data subsets to build regression trees
 189 that minimize errors in previous trees and are trained on a new data subset. Extra Trees
 190 Regressor uses highly randomized trees (Geurts et al., 2006) and data subsets to grow
 191 randomized regression trees with randomly selected split nodes. Each subsequent tree
 192 is fit on the negative gradient of the previous cost function. Model predictions are av-
 193 erages over the 100 (default) regression trees in the forest.

194 3.4 Feature Selection

195 Extra Tree Regression features are motivated by the equilibrium assumption that
 196 beach changes are driven by a disequilibrium between wave energy and bathymetry, with
 197 a time-lagged bathymetry response. Many potential features were explored. The selected
 198 six features are the preceding 12-hr average radiation stress S_{xx} , 30-day and 90-day wave
 199 energy anomaly mean and standard deviation, and previous beach width (Figure 5). Wave
 200 energy anomaly is wave energy minus the 2015 - 2022 mean. Observed, lagged correla-
 201 tions between seasonal shoreline change and time-averaged energy (Miller & Dean, 2007;
 202 Hansen & Barnard, 2010) are reproduced by an equilibrium model (Yates et al., 2011)
 203 so these features are equilibrium compatible but without the simplistic, arbitrary rules
 204 specifying the beach response to disequilibrium.

205 Wave energy anomaly means and standard deviation with 30- and 90-day windows
 206 are highly correlated (Figure 5 and Figure 6, $r^2=0.91$ between 30-day mean and 30-day
 207 standard deviation, and $r^2=0.94$ for the 90-day statistics). These correlations arise be-
 208 cause in southern California, storminess increases both the energy anomaly mean and
 209 standard deviation. Summer waves have low and relatively steady energy. During model
 210 training, the previous beach width is the observed value from the previous survey (Fig-
 211 ure 5b,f black line). In prediction mode, the trained ML model is initialized with a beach
 212 width observation and then steps forward in time using wave time series, similar to the
 213 Equilibrium model (Figure 2,3).

214 No single feature is essential to relatively successful ML performance, as all input
 215 features are highly correlated (or inversely correlated) with beach width (Figure 6). A
 216 subset of any four features has only a small reduction in skill (not shown). More sophis-
 217 ticated methods can be used to reduce feature redundancy.

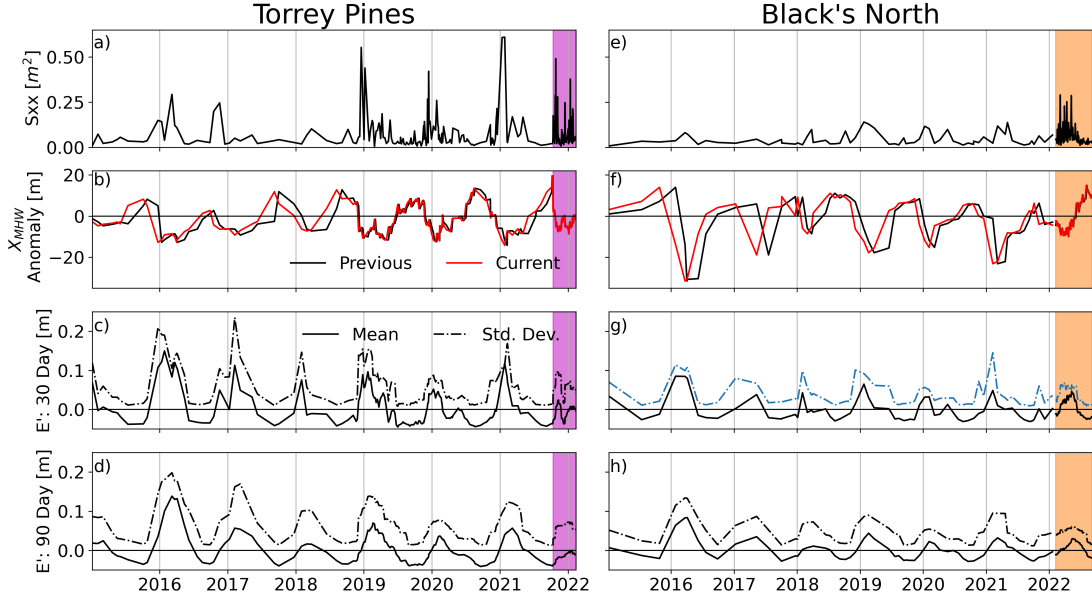


Figure 5. Time series of (a,e) S_{xx} (b,f) previous (black) and current (red) X_{MHW} anomaly (c,g) 30-day and (d,h) 90-day mean (solid) and standard deviation (dashed) of energy anomaly. Features (black) are used to predict current X_{MHW} anomaly (red) during the high frequency prediction period (magenta and orange boxes) at TP (left) and BN (right).

218

3.5 Machine Learning Performance

219

220

221

222

223

224

225

Torrey Pines MOP 581 during high-frequency sampling (Figure 5a-d, magenta box) is used to compare equilibrium and several ML models. The relatively large amount of training data ($N = 185$) includes a year of approximately weekly beach surveys (2019, Figure 2b,c). The trained ML and equilibrium models are assessed as predictive models (Tables 1,2). The input features include time series of wave statistics and an initial beach width. As a model steps forward in time, the previous beach width is updated with the model prediction.

226

227

228

229

230

231

Overall, extra tree (ET) slightly out performs the other supervised learning models with the lowest error (RMSE) and tied for the highest r^2 (Table 1). The Linear Regression model has an equivalent r^2 , but a persistent offset increases the bias and RMSE. Mean absolute error statistics (not shown) are consistent with RMSE. SVM fails to capture the extreme erosion of the initial event (not shown). ET was selected for further comparisons with the equilibrium model.

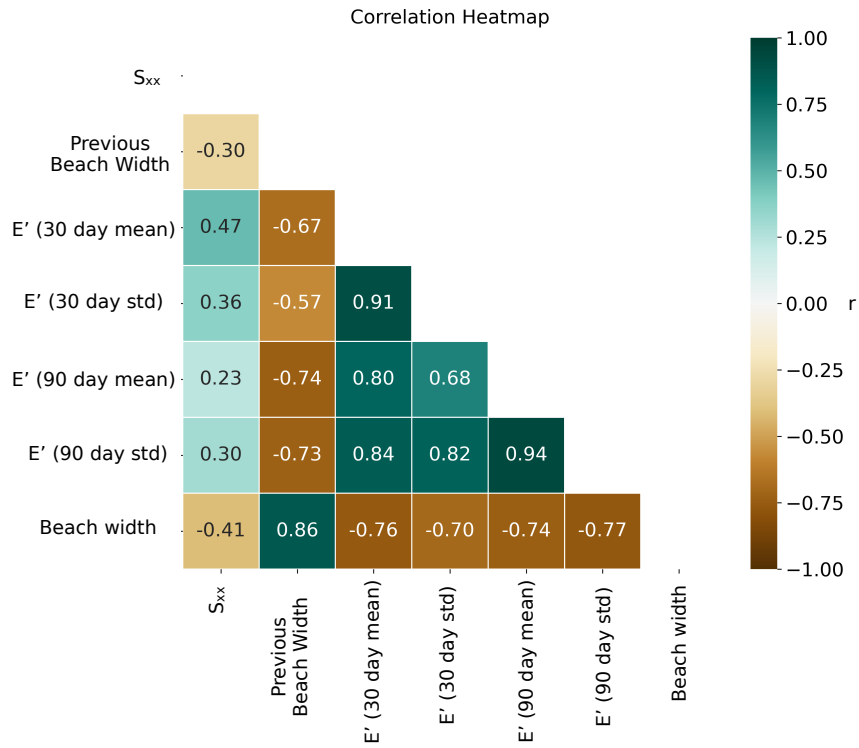


Figure 6. Correlation heat map of input features and beach width. Time series shown in Figure 5.

	RMSE, m	r^2	Bias, m
Linear	3.3	0.63	2.5
Support Vector	2.5	0.46	0.57
Decision Tree	3.0	0.42	0.83
Extra Trees	2.3	0.63	0.85
Gradient Boosting	2.5	0.50	0.35

Table 1. Errors, r^2 , and bias of supervised learning models for TP subweekly sampling.

4 Machine Learning vs. Equilibrium Model

The capabilities of ET and the equilibrium model are compared during two prediction periods. The first prediction is the high-frequency sampling periods at TP and BN (Figure 5, magenta and orange boxes, respectively). Observations from 2015 to the start of high frequency sampling are used for model training. The second prediction period spans the same four years (January 1, 2015 - December 21, 2018) at TP and BN, and observations from Jan 2019 - July 2022 are used for training (Figure 5). At TP the training data includes about one year of approximately weekly sampling.

The equilibrium model does not capture the large (15 m) erosion from the first event of the ‘21/‘22 winter (day 1-3, Figure 7a) and over-predicts erosion during the winter 2015-16 at TP (Figure 7b). These results could not be consistently improved with equilibrium model parameter tuning, but were improved with ML.

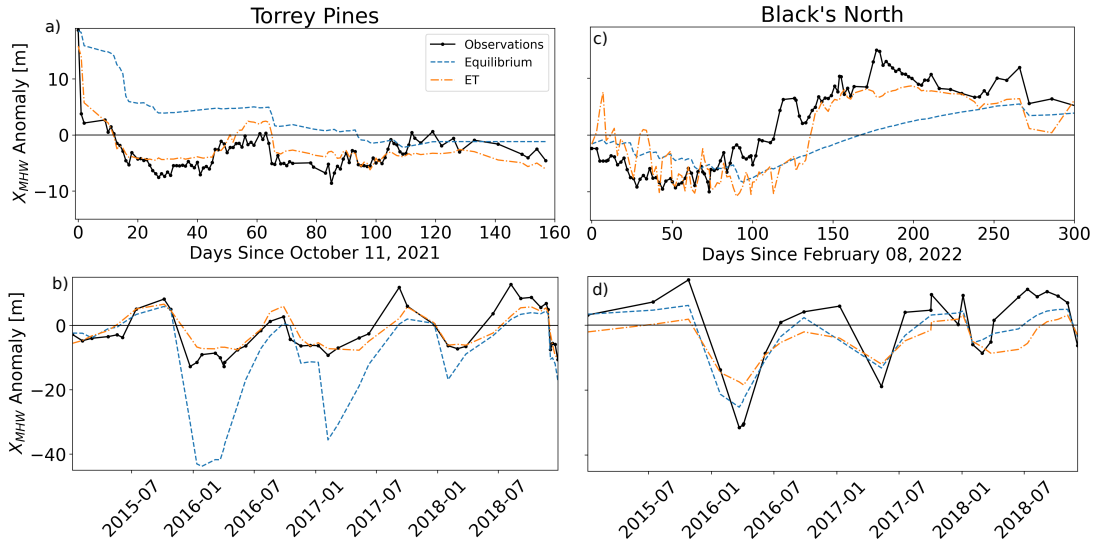


Figure 7. Time series of X_{MHW} anomaly observed (black line with dots) and modeled using the equilibrium model (blue dashed line) and Extra Trees Regressor (ET) model (orange dot-dash curve). (left) TP (MOP 581) and (right) BN (MOP 551). (top) sampled sub-weekly for 160 days at TP and 300 days at BN, and (bottom) roughly monthly for 2015-2018. At both beaches, ET outperforms equilibrium for the sub-weekly observations (Table 2).

At TP, ET outperforms the equilibrium model both during the 6-9 months of sub-weekly sampling and the four years (2015-2018) of less frequent sampling. RMSE with ET is reduced by more than 70% during both periods (Figure 6, Table 2). During the subweekly sampling, ET more accurately predicts the erosion during wave events, particularly during the first wave event (Figure 7a). At Tairua an equilibrium model is also relatively unresponsive to modest wave events that are better captured (Milke Index) by ML methods. However, ML had larger RMSE than equilibrium (table 3 in Gomez-de la Pena et al. (2023)). Furthermore, Equilibrium was tuned for minimum rmse and ML for optimal Milke index, complicating comparisons. At TP, ML clearly outperforms equilibrium independent of the error metric.

At BN, during sub-weekly sampling the ET model also out performs the equilibrium model with a smaller RMSE and larger r^2 (Figure 7c, Table 2). Qualitatively, both the ET and equilibrium models do not accrete as rapidly beginning around day 100; however, around day 140, ET rapidly accretes, reducing the misfit. In contrast to TP, the

258 equilibrium model outperforms ML from 2015-2018, with smaller RMSE and larger r^2
 259 (Table 2). The equilibrium model more closely predict the extreme erosion during the
 260 winter of ‘15-‘16, under predicted by ML by approximately 50%, presumably because
 261 extreme events are lacking in the training period. Qualitatively, ET and equilibrium mod-
 262 els correctly predict the most erosion during winter ‘15-‘16 and least erosion during win-
 263 ter ‘17-‘18. BN illustrates the increased importance of extensive training data to ML per-
 264 formance, relative to the limited training required by equilibrium models (Yates, Guza,
 265 & O’Reilly, 2009) and others .

	Torrey Pines		Black’s North	
	RMSE, m	r^2	RMSE, m	r^2
ET (HF)	2.2	0.63	3.7	0.66
Equilibrium (HF)	7.9	0.22	6.4	0.55
ET (2015-2018)	3.7	0.72	7.4	0.78
Equilibrium (2015-2018)	13.9	0.62	4.9	0.88

Table 2. Error (RMSE) and r^2 of ET and equilibrium models during the high-frequency HF (sub-weekly) test period (3-6 mo, Figure 3) and the 4-year test period (2015-2018).

266 4.1 ML Dependence on Training

267 The sensitivity of the ET model predictions to training data is assessed during the
 268 high-frequency sampling period at TP. Five restrictions to the training dataset are con-
 269 sidered: infrequent (> 30 days) surveys (Figure 8c), approximately weekly surveys for
 270 a limited time span (one year) (Figure 8d), only winter (Figure 8e), and only summer
 271 surveys (Figure 8f). Overall, ML performance is degraded when predictions are based
 272 on less complete training data. The full “all data” training period (Figure 8b) has the
 273 lowest RMSE and highest r^2 (Table 3). Additionally, the “all data” training yields re-
 274 sults most closely resembles the bi-modal shape of the year of sub-weekly observations.
 275 The strong performance of a winter training dataset, which includes a winter of weekly
 276 data, is consistent with the winter prediction period. Using only winter training peri-
 277 ods, ML produces only narrow beaches (Figure 8e), and thus, a negative bias (Table 3).
 278 Alternatively, only summer training data results in a large positive bias, although r^2 is
 only reduced by 20%

	RMSE, m	r^2	Bias
All data	2.3	0.63	0.85
> 30 days	2.8	0.49	1.9
\sim weekly	2.4	0.59	0.74
Only Winter	2.5	0.60	-0.15
Only Summer	4.1	0.50	3.4

Table 3. ET performance when modified training dataset includes only data observed greater than 30 days apart (row 2), only *weekly* data from 2019, during winter only, and during summer only.

280 Despite the limited (one year) time span, the weekly training data performs almost
 281 as well (similar RMSE, low bias and r^2) as the full “all data” training period (Table 3),
 282 highlighting the importance of high frequency training data. The result that 1 year of
 283 training suffices may be specific to TP-like beaches that reach the same annual minimum
 284 beach width due to a non-erodible back beach and/or cobble layer. The more complex
 285 interannual variability at BN presumably requires a wider variety of wave and beach con-
 286 ditions for skillful model training.

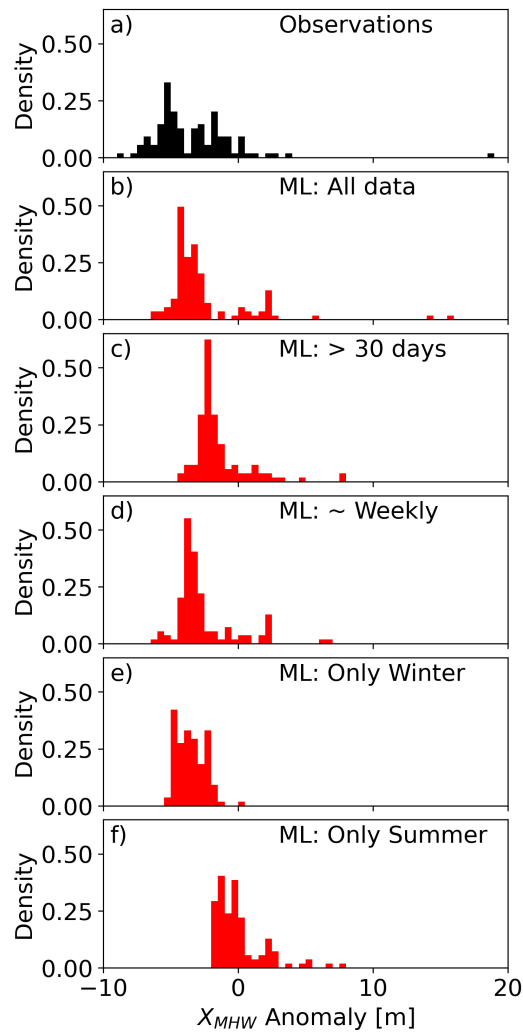


Figure 8. Torrey Pines MOP 581 during the sub-weekly prediction period. Histogram of (a) observations and (b - f) ML predictions trained on different observation subsets. Errors are in Table 3. Densities sum to 1.0 in each panel. ML predictions mirror the properties of the training data.

5 Conclusion

Changes in Mean High Water (MHW) location are tracked at sub-weekly and weekly time scales (Figure 7a,c). A generic equilibrium model replicates observed seasonal variations, but does not account for the cliff and rip rap back beach at TP and over predicts erosion during the 2016 El Niño (Figure 7b). An Extra Tree Regression (ET) model significantly outperforms the equilibrium model (Figure 7). Several (mutually) correlated features characterize the recent wave field (Figure 5), and recent waves are included simplistically as a 12-hr average S_{xx} . Future work includes developing ML estimators using different training features, sub-weekly training data that can resolve the observed 14-day slope variation, and new observations during extreme El Niño conditions.

Appendix A EOF analysis

Empirical orthogonal functions (EOF) decomposes time-space data into orthogonal basis functions that most efficiently captures the total variance. EOF 1 contains about 50 % of the total variance at TP and 93% at BN. EOF-1 is positive across the beach face at both sites, with a maximum $x \sim 70m$ at BN (Figure A1) where the terrace builds over the summer (Figure 4). At TP, the two largest changes in the mode-1 temporal amplitude coincide with narrowing of the beach and large waves with $H_s > 2$ m (Figure 3e). Mode-1 apparently excludes the 14-day tidal signal and provides a less obstructed view of beach evolution from the incident waves alone.

At BN, the temporal amplitude is negative during the winter and spring, when the subaerial beach is eroded, and then increases during summer and fall (Figure 3k). During winter, the equilibrium model and the mode-1 reconstruction show beach erosion response to individual storms (Figure 3l), but the model recovers less than observed.

At TP, significant variance (20%) is contained in mode-2 (Figure A2). Unlike the cross-shore uniform EOF-1, EOF-2 crosses zero between the mean location of MSL and MHW (Figure A2a). The temporal amplitude contains the 14-day tidal signal and fluctuates with the daily max tidal water level (Figure A2b). The mode-2 reconstruction (Figure A2c) shows that sand oscillates with 14-day period between the back and fore beach. During spring tide, sand moves seaward from the back to the fore beach, decreasing the slope. Conversely, during neap tide, sand moves from the fore to the back beach, steepening the beach.

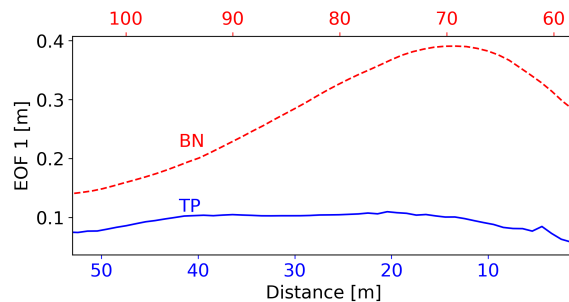


Figure A1. Subaerial EOF Mode-1: Spatial weight versus distance from the back beach origin. TP (blue solid) and BN (red dashed) contain 50% and 93% of the total variance, respectively. Weights are >0 .

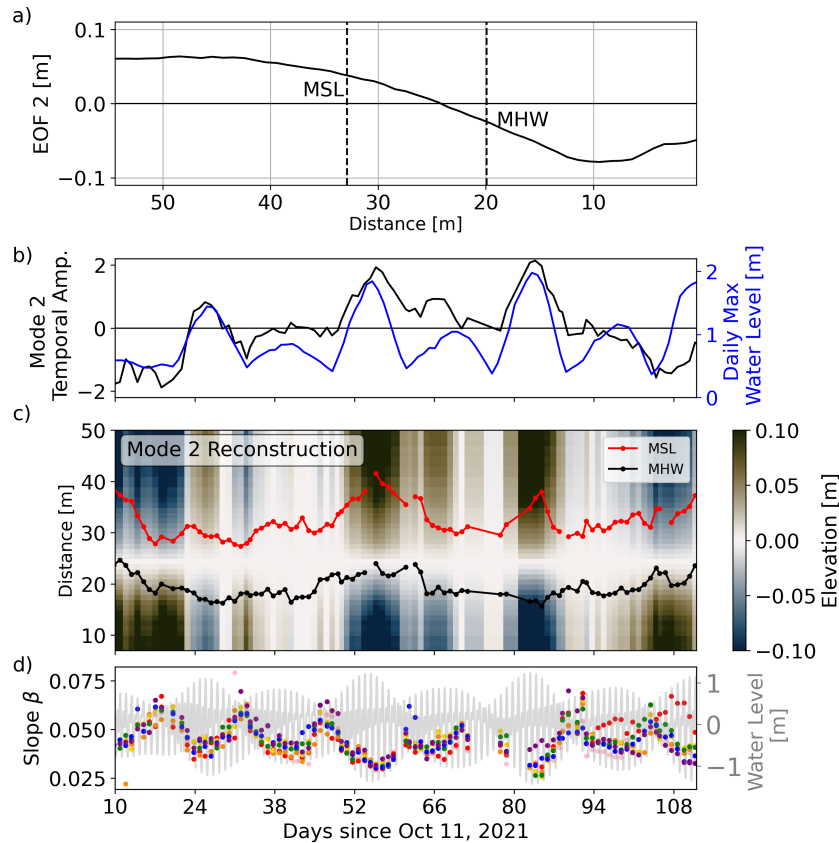


Figure A2. TP EOF Mode-2 contains 20% of the total variance. a) Mode-2 spatial weight versus distance from back beach origin. Spatial weight changes sign between X_{MSL} and X_{MHW} . (b) Mode-2 temporal EOF amplitude (black) and daily maximum water level (blue, right axis) versus time. (c) Mode-2 elevation reconstruction (color bar) versus cross-shore location and time. The distance between X_{MHW} (black) and X_{MSL} (red) contours vary with 14 day period. (d) beach slope β (colored dots correspond to different transects, see Figure 3 legend). Grey curve (right axis) is hourly tidal water level.

Open Research Section

The data necessary to reproduce results from this paper are currently available through Google Drive for the purposes of peer review https://drive.google.com/drive/folders/1ozuxQQIDWskc8g8EVNbwrfBmbVTxjg7h?usp=share_link, and will be publicly available through the University of California, San Diego library digital collections <https://library.ucsd.edu/dc/> (doi will be provided upon acceptance). Wave data is available at <https://cdip.ucsd.edu/>

Acknowledgments

This study was funded by the U.S. Army Corps of Engineers (W912HZ1920020) and the California Department of Parks and Recreation (C19E0026). Data were collected and processed by the Coastal Processes Group field team members Lucian Parry, Rob Grenzeback, Kent Smith, Brian Woodward, Greg Boyd, Shane Finnerty, Bill Boyd and others. Dr. Michele Okihiro organized and coordinated key aspects of the study, including the approximately 200 high frequency surveys. Thanks to all.

References

- 331
332 Athanasiou, P., van Dongeren, A., Giardino, A., Vousdoukas, M. I., Ranasinghe, R.,
333 & Kwadijk, J. (2020, 12). Uncertainties in projections of sandy beach erosion
334 due to sea level rise: an analysis at the European scale. *Scientific Reports*,
335 *10*(1). doi: 10.1038/s41598-020-68576-0
- 336 Blossier, B., Bryan, K. R., Daly, C. J., & Winter, C. (2017, 10). Shore and bar
337 cross-shore migration, rotation, and breathing processes at an embayed beach.
338 *Journal of Geophysical Research: Earth Surface*, *122*(10), 1745–1770. doi:
339 10.1002/2017JF004227
- 340 Breiman, L., Friedman, J., Olshen, R. A., & Stone, C. J. (2017). *Classification and*
341 *Regression Trees*. CRC Press.
- 342 Chang, C.-C., & Lin, C.-J. (2022, 8). *LIBSVM: A Library for Support Vector Ma-*
343 *chines* (Tech. Rep.). Taipei: National Taiwan University.
- 344 D’Anna, M., Castelle, B., Idier, D., Rohmer, J., Le Cozannet, G., Thieblemont,
345 R., & Bricheno, L. (2021, 8). Uncertainties in Shoreline Projections to 2100
346 at Truc Vert Beach (France): Role of Sea-Level Rise and Equilibrium Model
347 Assumptions. *Journal of Geophysical Research: Earth Surface*, *126*(8). doi:
348 10.1029/2021JF006160
- 349 Davidson, M. A., Splinter, K. D., & Turner, I. L. (2013). A simple equilibrium
350 model for predicting shoreline change. *Coastal Engineering*, *73*, 191–202.
351 Retrieved from [https://www.sciencedirect.com/science/article/pii/](https://www.sciencedirect.com/science/article/pii/S0378383912001676)
352 [S0378383912001676](https://www.sciencedirect.com/science/article/pii/S0378383912001676) doi: <https://doi.org/10.1016/j.coastaleng.2012.11.002>
- 353 Doria, A., Guza, R. T., O’Reilly, W. C., & Yates, M. L. (2016, 8). Observations and
354 modeling of San Diego beaches during El Niño. *Continental Shelf Research*,
355 *124*, 153–164. doi: 10.1016/j.csr.2016.05.008
- 356 Farris, A. S., & List, J. H. (2007, 5). Shoreline change as a proxy for subaerial beach
357 volume change. *Journal of Coastal Research*, *23*(3), 740–748. doi: 10.2112/05
358 -0442.1
- 359 Geurts, P., Ernst, D., & Wehenkel, L. (2006, 4). Extremely randomized trees. *Ma-*
360 *chine Learning*, *63*(1), 3–42. doi: 10.1007/s10994-006-6226-1
- 361 Gomez-de la Pena, E., Coco, G., Whittaker, C., & Montano, J. (2023). On the
362 use of Convolutional Deep Learning to predict shoreline change. *EGUsphere*
363 *[preprint]*, *2023*, 1–24. Retrieved from [https://egusphere.copernicus.org/](https://egusphere.copernicus.org/preprints/2023/egusphere-2023-958/)
364 [preprints/2023/egusphere-2023-958/](https://egusphere.copernicus.org/preprints/2023/egusphere-2023-958/) doi: 10.5194/egusphere-2023-958
- 365 Hansen, J. E., & Barnard, P. L. (2010, 11). Sub-weekly to interannual variability
366 of a high-energy shoreline. *Coastal Engineering*, *57*(11-12), 959–972. doi: 10
367 .1016/j.coastaleng.2010.05.011
- 368 Harley, M. D., Turner, I. L., Short, A. D., & Ranasinghe, R. (2011, 12). A reeval-
369 uation of coastal embayment rotation: The dominance of cross-shore versus
370 alongshore sediment transport processes, Collaroy-Narrabeen Beach, south-
371 east Australia. *Journal of Geophysical Research: Earth Surface*, *116*(4). doi:
372 10.1029/2011JF001989
- 373 Henderson, C. S., Fiedler, J. W., Merrifield, M. A., Guza, R. T., & Young, A. P.
374 (2022, 8). Phase resolving runup and overtopping field validation of SWASH.
375 *Coastal Engineering*, *175*. doi: 10.1016/j.coastaleng.2022.104128
- 376 Kalligeris, N., Smit, P. B., Ludka, B. C., Guza, R. T., & Gallien, T. W. (2020,
377 6). Calibration and assessment of process-based numerical models for beach
378 profile evolution in southern California. *Coastal Engineering*, *158*. doi:
379 10.1016/j.coastaleng.2020.103650
- 380 Ludka, B. C., Guza, R. T., O’Reilly, W. C., & Yates, M. L. (2015). Field evi-
381 dence of beach profile evolution toward equilibrium. *Journal of Geophys-*
382 *ical Research: Oceans*, *120*(11), 7574–7597. Retrieved from [https://](https://agupubs.onlinelibrary.wiley.com/doi/abs/10.1002/2015JC010893)
383 agupubs.onlinelibrary.wiley.com/doi/abs/10.1002/2015JC010893 doi:
384 <https://doi.org/10.1002/2015JC010893>
- 385 Matsumoto, H., & Young, A. P. (2022, 12). Quantitative regional observations of

- 386 gravel and bedrock influence on beach morphologies. *Geomorphology*, 419. doi:
387 10.1016/j.geomorph.2022.108491
- 388 Matsumoto, H., Young, A. P., & Guza, R. T. (2020). Cusp and Mega Cusp
389 Observations on a Mixed Sediment Beach. Retrieved from [https://](https://agupubs.onlinelibrary.wiley.com/doi/10.1029/2020EA001366)
390 agupubs.onlinelibrary.wiley.com/doi/10.1029/2020EA001366 doi:
391 10.1029/2020EA001366-T
- 392 Miller, J. K., & Dean, R. G. (2004). A simple new shoreline change model. *Coastal*
393 *Engineering*, 51(7), 531–556. Retrieved from [https://www.sciencedirect](https://www.sciencedirect.com/science/article/pii/S0378383904000614)
394 [.com/science/article/pii/S0378383904000614](https://www.sciencedirect.com/science/article/pii/S0378383904000614) doi: [https://doi.org/](https://doi.org/10.1016/j.coastaleng.2004.05.006)
395 10.1016/j.coastaleng.2004.05.006
- 396 Miller, J. K., & Dean, R. G. (2007, 2). Shoreline variability via empirical orthogo-
397 nal function analysis: Part II relationship to nearshore conditions. *Coastal En-*
398 *gineering*, 54(2), 133–150. doi: 10.1016/j.coastaleng.2006.08.014
- 399 Montaña, J., Coco, G., Antolínez, J. A., Beuzen, T., Bryan, K. R., Cagigal, L., ...
400 Vos, K. (2020, 12). Blind testing of shoreline evolution models. *Scientific*
401 *Reports*, 10(1). doi: 10.1038/s41598-020-59018-y
- 402 Muñoz-Pérez, J. J., & Medina, R. (2000). *Profile Changes due to a Fortnightly Tidal*
403 *Cycle* (Tech. Rep.).
- 404 O'Reilly, W. C., Olfe, C. B., Thomas, J., Seymour, R. J., & Guza, R. T. (2016).
405 The California coastal wave monitoring and prediction system. *Coastal En-*
406 *gineering*, 116, 118–132. Retrieved from [https://www.sciencedirect.com/](https://www.sciencedirect.com/science/article/pii/S0378383916301120)
407 [science/article/pii/S0378383916301120](https://www.sciencedirect.com/science/article/pii/S0378383916301120) doi: [https://doi.org/10.1016/](https://doi.org/10.1016/j.coastaleng.2016.06.005)
408 [j.coastaleng.2016.06.005](https://doi.org/10.1016/j.coastaleng.2016.06.005)
- 409 Pedregosa, F., Michel, V., Grisel, O., Blondel, M., Prettenhofer, P., Weiss, R.,
410 ... Duchesnay, (2011). Scikit-learn: Machine Learning in Python.
411 *Journal of Machine Learning Research*, 12, 2825–2830. Retrieved from
412 <http://scikit-learn.sourceforge.net>.
- 413 Phillips, M. S., Harley, M. D., Turner, I. L., Splinter, K. D., & Cox, R. J. (2017,
414 3). Shoreline recovery on wave-dominated sandy coastlines: the role of sand-
415 bar morphodynamics and nearshore wave parameters. *Marine Geology*, 385,
416 146–159. doi: 10.1016/j.margeo.2017.01.005
- 417 Rahimi, A., & Recht, B. (2007). Random Features for Large-Scale Kernel Machines.
418 In J. Platt, D. Koller, Y. Singer, & S. Roweis (Eds.), *Advances in neural in-*
419 *formation processing systems* (Vol. 20). Curran Associates, Inc. Retrieved
420 from [https://proceedings.neurips.cc/paper_files/paper/2007/file/](https://proceedings.neurips.cc/paper_files/paper/2007/file/013a006f03dbc5392effeb8f18fda755-Paper.pdf)
421 [013a006f03dbc5392effeb8f18fda755-Paper.pdf](https://proceedings.neurips.cc/paper_files/paper/2007/file/013a006f03dbc5392effeb8f18fda755-Paper.pdf)
- 422 Ruggerio, P., Kratzmann, M. G., Himmelstoss, E. A., Reid, D., Allan, J., & Kamin-
423 sky, G. (2013). *National assessment of shoreline change: historical shoreline*
424 *change along the Pacific Northwest coast* (Tech. Rep.). Reston, VA. Re-
425 trieved from <http://pubs.er.usgs.gov/publication/ofr20121007> doi:
426 10.3133/ofr20121007
- 427 Ruggiero, P., Buijsman, M., Kaminsky, G. M., & Gelfenbaum, G. (2010). Model-
428 ing the effects of wave climate and sediment supply variability on large-scale
429 shoreline change. *Marine Geology*, 273(1), 127–140. Retrieved from [https://](https://www.sciencedirect.com/science/article/pii/S0025322710000708)
430 www.sciencedirect.com/science/article/pii/S0025322710000708 doi:
431 <https://doi.org/10.1016/j.margeo.2010.02.008>
- 432 Sallenger, A. H., Krabill, W., Brock, J., Swift, R., Manizade, S., & Stockdon,
433 H. (2002). *Sea-cliff erosion as a function of beach changes and extreme*
434 *wave runup during the 1997-1998 El Niño* (Tech. Rep.). Retrieved from
435 www.elsevier.com/locate/margeo
- 436 Simmons, J. A., & Splinter, K. D. (2022, 4). A multi-model ensemble approach to
437 coastal storm erosion prediction. *Environmental Modelling and Software*, 150.
438 doi: 10.1016/j.envsoft.2022.105356
- 439 Splinter, K. D., Turner, I. L., Davidson, M. A., Barnard, P., Castelle, B., &
440 Oltman-Shay, J. (2014). A generalized equilibrium model for predict-

- 441 ing daily to interannual shoreline response. *Journal of Geophysical Re-*
442 *search: Earth Surface*, 119(9), 1936–1958. Retrieved from [https://](https://agupubs.onlinelibrary.wiley.com/doi/abs/10.1002/2014JF003106)
443 agupubs.onlinelibrary.wiley.com/doi/abs/10.1002/2014JF003106 doi:
444 <https://doi.org/10.1002/2014JF003106>
- 445 Straub, J. A., Rodriguez, A. B., Luettich, R. A., Moore, L. J., Itzkin, M., Ridge,
446 J. T., ... Theuerkauf, E. J. (2020, 7). The role of beach state and the timing
447 of pre-storm surveys in determining the accuracy of storm impact assessments.
448 *Marine Geology*, 425. doi: 10.1016/j.margeo.2020.106201
- 449 Wright, L. D., Short, A. D., & Green, M. O. (1985). Short-term changes in
450 the morphodynamic states of beaches and surf zones: An empirical predic-
451 tive model. *Marine Geology*, 62(3), 339–364. Retrieved from [https://](https://www.sciencedirect.com/science/article/pii/0025322785901239)
452 www.sciencedirect.com/science/article/pii/0025322785901239 doi:
453 [https://doi.org/10.1016/0025-3227\(85\)90123-9](https://doi.org/10.1016/0025-3227(85)90123-9)
- 454 Yates, M. L., Guza, R. T., & O'Reilly, W. C. (2009). Equilibrium shoreline re-
455 sponse: Observations and modeling. *Journal of Geophysical Research: Oceans*,
456 114(C9). Retrieved from [https://agupubs.onlinelibrary.wiley.com/doi/](https://agupubs.onlinelibrary.wiley.com/doi/abs/10.1029/2009JC005359)
457 [abs/10.1029/2009JC005359](https://agupubs.onlinelibrary.wiley.com/doi/abs/10.1029/2009JC005359) doi: <https://doi.org/10.1029/2009JC005359>
- 458 Yates, M. L., Guza, R. T., O'Reilly, W. C., Hansen, J. E., & Barnard, P. L. (2011).
459 Equilibrium shoreline response of a high wave energy beach. *Journal of Geo-*
460 *physical Research: Oceans*, 116(4). doi: 10.1029/2010JC006681
- 461 Yates, M. L., Guza, R. T., O'Reilly, W. C., & Seymour, R. J. (2009). Overview of
462 seasonal sand level changes on southern California Beaches. *Shore & Beaches*,
463 77(1), 39–46.